Numerical Solutions of the Navier-Stokes Equations for Transonic Afterbody Flows

R. Charles Swanson, Jr.

DECEMBER 1980

NASA

NASA Technical Paper 1784

Numerical Solutions of the Navier-Stokes Equations for Transonic Afterbody Flows

R. Charles Swanson, Jr.
Langley Research Center
Hampton, Virginia

SUMMARY

The time-dependent Navier-Stokes equations in mass-averaged variables are
solved for transonic flow over axisymmetric boattail-plume simulator configura-
tions. Numerical solution of these equations is accomplished with the unsplit
explicit finite-difference algorithm of MacCormack. A grid subcycling procedure
and computer code vectorization are used to improve computational efficiency.
The two-layer algebraic turbulence models of Cebeci-Smith and Baldwin-Lomax are
employed for investigating turbulence closure. Two relaxation models based on
these baseline models are also considered. Results in the form of surface-
pressure distributions for three different circular-arc boattails at two free-
stream Mach numbers ($M_\infty = 0.8$ and 1.3) are compared with experimental data.
The pressures in the recirculating flow region for all separated cases are
poorly predicted with the baseline turbulence models. Significant improvements
in the predictions are usually obtained by using the relaxation models.

INTRODUCTION

The drag of the afterbody of a fighter aircraft represents a significant
part (approximately 30 to 40 percent) of the total configuration drag at tran-
sonic speeds. The external geometry of the jet-exhaust nozzle has a strong
impact on the drag of the afterbody. Consequently, considerable emphasis is
placed upon optimizing the design of this component of the aircraft afterbody.
Because of the complex nature of the nozzle-boattail/jet-exhaust flow, which can
include strong viscous-inviscid and shock—boundary-layer interactions, para-
metric wind-tunnel testing is employed to provide data bases for the design
process. Wind-tunnel models, especially those which have exhaust jets, are
complicated and expensive. In order to minimize the number of required experi-
ments to determine aft-end aerodynamic characteristics, reliable theoretical
techniques are needed.

One approach to the solution of the axisymmetric nozzle-afterbody/jet-
exhaust problem involves a decomposition of the flow field and a subsequent
patching together of the individual components. This dissection of the flow
field generally includes the boattail boundary layer, inviscid jet, exhaust
shear layer, and inviscid external flow. The basic mechanism for coupling these
flow-field elements is the interaction, which is assumed to be weak, between
inviscid and viscous flow regions (i.e., displacement thickness concept).
Interactive effects are taken into account with an iterative procedure. Several
investigators (refs. 1 to 4) have obtained good comparisons between predictions
and experimental data for the nozzle-boattail pressure distribution when the
free-stream flow is subsonic, the boundary layer is turbulent and attached, and
the exhaust flow is simulated (i.e., solid-plume simulator to represent ideally
or nearly ideally expanded jets) or high-pressure air. Some computations
(refs. 5 and 6) have also been made for separated flow on boattail configura-
tions. In reference 5 the separation location is obtained from experimental
data, and the shape of the outer boundary of the recirculating flow region

(discriminating streamline) is assumed and held constant throughout the viscous-inviscid interaction calculation. In reference 6, the separation location is computed through the application of an inverse boundary-layer technique. The discriminating streamline is assumed to be conical in shape, and its slope is determined in the interaction procedure. The weak-interaction assumption is made with both of these solution methods. Using these approaches the predicted pressure variations generally agree fairly well with laboratory data for sub-critical flows; the largest differences are usually either in the separated-flow region or in the vicinity of reattachment. For supercritical flows the agreement between theory and experiment is not as good and deteriorates with increases in Mach number. This is to be expected because of the strong inter-action due to the presence of a shock. These results for separated flows suggest that difficulties would exist in extending the weak-interaction theory to general three-dimensional afterbody flows.

Another approach that is currently being applied to the afterbody problem is the solution of the time-dependent Navier-Stokes equations. There are no assumptions made about the type of interactions present in the flow field, and the viscous and inviscid flow regions are computed simultaneously. The steady-state solution for the flow is obtained as the time asymptotic limit. Holst (ref. 7) has calculated surface pressure-coefficient distributions for axisym-metric boattail-plume simulator geometries when the free stream is supersonic and the boundary layer is turbulent. These results generally agree well with experiment. The pressures in the separation region are consistently overpre-dicted. This is attributed to turbulence modeling. Subsequently, Mikhail, Hankey, and Shang (ref. 8) computed supersonic flow over nozzle afterbodies with hot or cold supersonic jets. Since these results were obtained primarily to demonstrate computational capability, the accuracy is not sufficient for good predictions. However, the trends of the experimental data are captured. More recently, Jacocks (ref. 9) and Deiwert (ref. 10) obtained solutions for subsonic flow past some boattail-plume simulator configurations. Surface-pressure results compare favorably with experimental data. Once again, in the case of separated flows, the largest differences appear in the reverse-flow region.

In the present application the time-dependent, axisymmetric, compressible, mass-averaged Navier-Stokes equations are solved for transonic flow (both sub-sonic and supersonic) over nozzle afterbodies. In order to isolate the separa-tion problem from jet-mixing effects, a solid-plume simulator is used to model the jet exhaust. Reubush (ref. 11) demonstrated the validity of using solid cylinders to simulate perfectly or nearly perfectly expanded jets when entrain-ment effects are not important. Because upstream feeding is present in subsonic flows, special attention is directed towards establishing an appropriate set of boundary conditions for the mathematical problem. At the time this work was undertaken, no subsonic calculations for afterbody flows using the Navier-Stokes equations had been reported. The equations are solved with the unsplit explicit numerical algorithm of MacCormack (ref. 12). In order to enhance computational efficiency, especially for subsonic flows, the finite-difference scheme is coded for the Control Data CYBER 203 computer system. A grid subcycling pro-cedure is employed also to improve computing time. To close the set of governing equations, turbulence modeling is implemented.

From previous Navier-Stokes work, turbulence modeling generally seems to be the culprit for poor turbulent-flow predictions. Therefore, some special attention is dedicated to this aspect of the problem. At this time, one-equation and two-equation models for the turbulence transport processes have not been adequately shown to provide the best turbulence closure. Since a substantial increase in computational time results when these models are applied, only algebraic turbulence models are considered in this investigation. The two-layer model of Cebeci and Smith (ref. 13) and the two-layer model of Baldwin and Lomax (ref. 14) are considered. Both of these models are applied with and without the addition of a turbulence lag model (ref. 15), which is used to account for upstream history effects on the turbulence. The afterbody surface-pressure distributions obtained using these models are compared with experimental data.

SYMBOLS

a	speed of sound, $\hat{a}/\hat{u}_\infty$
c_p	pressure coefficient
$\hat{c}_p, \hat{c}_v$	specific-heat coefficients
$\hat{d}_e$	boattail-exit diameter, 0.0762 meter
d_m	maximum diameter of boattail, $\hat{d}_m/\hat{d}_e = 2.0$
E	total internal energy per unit volume, $\hat{E}/(\hat{\rho}_\infty \hat{u}_\infty{}^2)$
K	Von Karman constant
$\hat{k}$	coefficient of thermal conductivity
$\hat{k}_T$	eddy thermal conductivity
ℓ	ratio of boattail length to boattail-exit diameter, $\hat{\ell}/\hat{d}_e$
M	Mach number
$N_{Pr,m}$	molecular Prandtl number, $\hat{c}_p\hat{\mu}/\hat{k}$
$N_{Pr,t}$	turbulent Prandtl number, $\hat{c}_p\hat{\epsilon}/\hat{k}_T$
N_{Re}	Reynolds number, $\hat{\rho}_\infty \hat{u}_\infty \hat{d}_e/\hat{\mu}_{ref}$
p	pressure, $\hat{p}/(\hat{\rho}_\infty \hat{u}_\infty{}^2)$
q_i	heat-flux vector
R	reattachment location
r_c	radius of curvature of boattail, $\hat{r}_c/\hat{d}_e$

r_B body radius, $\hat{r}_B/\hat{d}_e$

s separation location

T temperature, $\hat{T}/(\hat{u}_\infty^2/\hat{C}_v) = \hat{T}/\hat{T}_{ref}$

u,v axial and radial velocity components, $\hat{u}/\hat{u}_\infty,\ \hat{v}/\hat{u}_\infty$

x,y,t independent variables (computational domain), $\hat{x}/\hat{d}_e,\ \hat{y}/\hat{d}_e,\ \hat{t}\hat{u}_\infty/\hat{d}_e$

$\bar{y}$ normal distance from wall, $\hat{\bar{y}}/\hat{d}_e$

$\bar{y}^+$ dimensionless distance from the wall $\left(\bar{y}^+ = \sqrt{|\tau_w|\rho_w}\,(\bar{y}/\mu_w)\,N_{Re}\right)$

z,r,t independent variables (physical domain), $\hat{z}/\hat{d}_e,\ \hat{r}/\hat{d}_e,\ \hat{t}\hat{u}_\infty/\hat{d}_e$

z_I z at initiation of relaxation

β_c chord boattail angle

γ ratio of specific heats, $\hat{C}_p/\hat{C}_v$

$\Delta x,\Delta y,\Delta t$ finite-difference increments (computational domain)

$\Delta z,\Delta r,\Delta t$ finite-difference increments (physical domain)

δ local boundary-layer thickness, $\hat{\delta}/\hat{d}_e$

δ_I local boundary-layer thickness at initiation of relaxation

ε eddy viscosity, $\hat{\varepsilon}/\hat{\mu}_{ref}$

$\bar{\theta}$ flow inclination angle

λ relaxation-length parameter, $\hat{\lambda}/\hat{d}_e$

μ coefficient of molecular viscosity, $\hat{\mu}/\hat{\mu}_{ref}$

ρ density, $\hat{\rho}/\hat{\rho}_\infty$

τ shear stress, $\hat{\tau}/(\hat{\rho}_\infty\hat{u}_\infty^2)$

τ_{ij} shear tensor

Subscripts:

e edge conditions

exp   experimental conditions

i,j x,y grid indices

4

max   maximum conditions

min   minimum conditions

ref   reference conditions

t   total conditions

w   wall conditions

x,y,z,r   differentiation with respect to x, $\dot{y}$, z, and r

∞   free-stream conditions

Superscript:

n   time-step index

Turbulence model designations:

B-L   Baldwin-Lomax model

C-S   Cebeci-Smith model

R(B-L)   Baldwin-Lomax model with relaxation

R(C-S)   Cebeci-Smith model with relaxation

Other notation:

Circumflex over symbol (i.e., $\hat{\rho}$) denotes dimensional variable

ANALYSIS

Governing Flow Equations

Solutions for turbulent, viscous, transonic flow over axisymmetric after-body configurations are obtained by solving the equations for conservation of mass, momentum, and energy. The governing equations are first written in terms of the instantaneous flow quantities of pressure, density, velocity, and total internal energy. The dependent variables p, ρ are replaced by Reynolds expansions (sum of mean-flow component and fluctuating component). The remaining flow quantities are expanded in terms of mass-averaged variables. Reference 16 contains additional details concerning mass-averaged variables. The equations are time-averaged in the usual sense. The resulting turbulent-flow equations have the same form as their laminar-flow counterparts, except the stress tensor is augmented by the Reynolds stress tensor, and the heat-flux vector is augmented by the additional heat-flux terms associated with the turbulence. Using the eddy-viscosity hypothesis, this effectively means the

eddy viscosity is added to the molecular viscosity, and the eddy thermal con-
ductivity is added to the molecular thermal conductivity. Thus, the time-
dependent Navier-Stokes equations (written in axisymmetric coordinates and in
nondimensional form) for a turbulent, compressible flow in which body forces
are neglected are

$$\frac{\partial U}{\partial t} + \frac{\partial F}{\partial z} + \frac{\partial G}{\partial r} + H = 0 \tag{1a}$$

where

$$U = r \begin{bmatrix} \rho \\ \rho u \\ \rho v \\ E \end{bmatrix} \tag{1b}$$

$$F = r \begin{bmatrix} \rho u \\ \rho u^2 - \tau_{zz} \\ \rho u v - \tau_{zr} \\ Eu - \tau_{zz} u - \tau_{zr} v + q_z \end{bmatrix} \tag{1c}$$

$$G = r \begin{bmatrix} \rho v \\ \rho u v - \tau_{rz} \\ \rho v^2 - \tau_{rr} \\ Ev - \tau_{rz} u - \tau_{rr} v + q_r \end{bmatrix} \tag{1d}$$

$$H = \begin{bmatrix} 0 \\ 0 \\ \tau_{\theta\theta} \\ 0 \end{bmatrix} \tag{1e}$$

6

$$E = \rho\left(T + \frac{u^2 + v^2}{2}\right) \tag{1f}$$

The elements of the stress tensor and heat-flux vector are given by

$$\left.\begin{array}{l} \tau_{zz} = -p - \dfrac{2}{3}\left(\dfrac{\mu + \varepsilon}{N_{Re}}\right)\left(\dfrac{\partial v}{\partial r} + \dfrac{v}{r}\right) + \dfrac{4}{3}\left(\dfrac{\mu + \varepsilon}{N_{Re}}\right)\dfrac{\partial u}{\partial z} \\[12pt] \tau_{rr} = -p - \dfrac{2}{3}\left(\dfrac{\mu + \varepsilon}{N_{Re}}\right)\left(\dfrac{\partial u}{\partial z} + \dfrac{v}{r}\right) + \dfrac{4}{3}\left(\dfrac{\mu + \varepsilon}{N_{Re}}\right)\dfrac{\partial v}{\partial r} \\[12pt] \tau_{\theta\theta} = -p - \dfrac{2}{3}\left(\dfrac{\mu + \varepsilon}{N_{Re}}\right)\left(\dfrac{\partial u}{\partial z} + \dfrac{\partial v}{\partial r}\right) + \dfrac{4}{3}\left(\dfrac{\mu + \varepsilon}{N_{Re}}\right)\dfrac{v}{r} \\[12pt] \tau_{rz} = \tau_{zr} = \left(\dfrac{\mu + \varepsilon}{N_{Re}}\right)\left(\dfrac{\partial u}{\partial r} + \dfrac{\partial v}{\partial z}\right) \end{array}\right\} \tag{2}$$

$$\left.\begin{array}{l} q_z = - \dfrac{\gamma}{N_{Re}}\left(\dfrac{\mu}{N_{Pr,m}} + \dfrac{\varepsilon}{N_{Pr,t}}\right)\dfrac{\partial T}{\partial z} \\[14pt] q_r = - \dfrac{\gamma}{N_{Re}}\left(\dfrac{\mu}{N_{Pr,m}} + \dfrac{\varepsilon}{N_{Pr,t}}\right)\dfrac{\partial T}{\partial r} \end{array}\right\} \tag{3}$$

The flow quantities and independent variables are nondimensionalized in the following way:

$$\left.\begin{array}{lll} \rho = \hat{\rho}/\hat{\rho}_\infty & p = \hat{p}/\hat{p}_{ref} & T = \hat{T}/\hat{T}_{ref} \\[10pt] \mu = \hat{\mu}/\hat{\mu}_{ref} & \varepsilon = \hat{\varepsilon}/\hat{\mu}_{ref} & u = \hat{u}/\hat{u}_\infty \\[10pt] v = \hat{v}/\hat{u}_\infty & E = \hat{E}/\hat{p}_{ref} & z = \hat{z}/\hat{d}_e \\[10pt] r = \hat{r}/\hat{d}_e & t = \hat{t}\hat{u}_\infty/\hat{d}_e & \end{array}\right\} \tag{4a}$$

The reference quantities are given by

$$\left.\begin{array}{ll} \hat{p}_{ref} = \hat{\rho}_\infty\hat{u}_\infty^2 & \hat{T}_{ref} = \hat{u}_\infty^2/\hat{C}_v \\[10pt] \hat{\mu}_{ref} = c_1\hat{T}_{ref}^{3/2}/\left(\hat{T}_{ref} + c_2\right) & N_{Re} = \hat{\rho}_\infty\hat{u}_\infty\hat{d}_e/\hat{\mu}_{ref} \end{array}\right\} \tag{4b}$$

where C_1 and C_2 are constants. The gas is assumed to be thermally and calorically perfect. Thus,

$$p = (\gamma - 1)\rho T \tag{5}$$

and the specific heats $\hat{C}_p$ and $\hat{C}_v$ are constants. The molecular viscosity is evaluated with Sutherland's law as follows:

$$\mu = C_1 T^{3/2} \Big/ (T + C_2) \tag{6}$$

The molecular Prandtl number and turbulent Prandtl number are assumed to be constant at 0.72 and 0.9, respectively.

Coordinate Transformation

In order to facilitate the implementation of the finite-difference formulation for solving equation (1a) and the treatment of the boundary conditions, a body-fitted curvilinear coordinate transformation is employed. This transformation maps the physical flow region (fig. 1) in the z,r plane onto a rectangular computational region, which has uniformly spaced grid lines, in an x,y plane. Using the chain rule for partial differentiation, the governing vector equation takes the following quasi-conservative form:

$$\frac{\partial U}{\partial t} + x_z \frac{\partial F}{\partial x} + x_r \frac{\partial G}{\partial x} + y_z \frac{\partial F}{\partial y} + y_r \frac{\partial G}{\partial y} + H = 0 \tag{7}$$

The derivatives in the definitions of the components of the stress tensor and heat-flux vector are expanded in the same manner. The transformation derivatives x_z, x_r, y_z, and y_r are determined from the relations

$$\left. \begin{array}{ll} x_z = Jr_y & y_z = -Jr_x \\[2ex] x_r = -Jz_y & y_r = Jz_x \\[2ex] J = x_z y_r - x_r y_z = 1 \Big/ (z_x r_y - z_y r_x) \end{array} \right\} \tag{8}$$

where the subscripts indicate partial differentiation, and where J is the transformation Jacobian. The derivatives are computed numerically.

Grid Generation

The Thompson, Thames, and Mastin (ref. 17) method is currently being used to produce grids for finite-difference calculations for a wide variety of fluid

8

dynamics problems. With this technique, the relationship between grid points in an arbitrary physical flow region and the corresponding known grid points in a rectangular computational domain is obtained by solving an elliptic system of partial differential equations. In terms of the independent variables of the transformation applied herein $(z,r) \rightarrow (x,y)$, the mesh-generating equations are

$$x_{zz} + x_{rr} = P(x,y) \tag{9a}$$

$$y_{zz} + y_{rr} = Q(x,y) \tag{9b}$$

where $P(x,y)$ and $Q(x,y)$ are source terms used to control interior grid-line spacing. The finite-difference solution of equations (9a) and (9b) is simplified by reversing the roles of the independent and dependent variables and solving the resulting quasi-linear elliptic system. The quasi-linear equations

$$\alpha z_{xx} - 2\beta z_{xy} + \zeta z_{yy} = -J^2(Pz_x + Qz_y) \tag{10a}$$

$$\alpha r_{xx} - 2\beta r_{xy} + \zeta r_{yy} = -J^2(Pr_x + Qr_y) \tag{10b}$$

where

$$\left.\begin{array}{l}
\alpha = z_y{}^2 + r_y{}^2 \\[2mm]
\beta = z_x z_y + r_x r_y \\[2mm]
\zeta = z_x{}^2 + r_x{}^2
\end{array}\right\} \tag{10c}$$

are solved on the same rectangular grid with a square mesh ($\Delta x = \Delta y = 1$) as the flow equations. The coordinates of the grid points on the boundaries of the physical flow region provide the boundary conditions for the elliptic problem in the computational plane.

In the Thompson, Thames, and Mastin (TTM) procedure the source terms are combinations of exponential functions, and they include parameters to control their effect. These parameters are problem sensitive. To circumvent this deficiency, Thomas (ref. 18) uses source quantities with special properties. The functions are

$$\left.\begin{array}{l}
P(x,y) = \phi(x,y)\left(x_z{}^2 + x_r{}^2\right) \\[3mm]
Q(x,y) = \psi(x,y)\left(y_z{}^2 + y_r{}^2\right)
\end{array}\right\} \tag{11}$$

9

When P and Q are substituted into equations (9a) and (9b), the elliptic system in the transformed plane is

$$\alpha(z_{xx} + \phi z_x) - 2\beta z_{xy} + \zeta(z_{yy} + \psi z_y) = 0 \qquad (12a)$$

$$\alpha(r_{xx} + \phi r_x) - 2\beta r_{xy} + \zeta(r_{yy} + \psi r_y) = 0 \qquad (12b)$$

and $\phi(x,y)$ and $\psi(x,y)$ are parameters. These equations possess exponential solutions for locally constant ϕ and ψ. The parameters ϕ and ψ are determined at the boundaries of the computational region by solving the limiting forms of equations (12a) and (12b) at the boundaries. The interior values are obtained by linear interpolation along constant coordinate lines (i.e., x = Constant and y = Constant) between boundaries. With this approach, the interior grid-point spacing reflects the distributions of the boundary points.

For the afterbody flows being considered, the TTM method is applied with the source functions of reference 18. The grid points at the inflow and outflow boundaries of the physical domain are distributed exponentially in the radial direction. Consequently, the surface viscous layer can be adequately resolved, and fine-grid spacing is not present where it is not needed (i.e., inviscid flow). Since the pressure gradients for the boattail portion of the afterbody flow can be substantial, the grid points in the axial direction are clustered about a point on the boattail using a stretching function constructed with polynomials. The cluster point is located in the interval 0.6ℓ to ℓ. The location is a function of the free-stream Mach number. In this manner good resolution can be obtained not only in the boattail region but also in the juncture region of the boattail and plume simulator. The ratio $\Delta z_{max}/\Delta z_{min}$ varies from about 3 to 6, depending upon ℓ, Δz_{max} ($0.3 \leq \Delta z_{max} \leq 0.45$), and the length of the afterbody. A typical grid in the physical domain is shown in figure 2.

Boundary Conditions

In order to complete the mathematical formulation for the physical problem under consideration, an appropriate set of boundary conditions must be specified. There are four boundaries for the flow region associated with the afterbody (see fig. 1). At the afterbody surface (cylinder-boattail-cylinder configuration), the no-slip condition and a wall temperature are imposed. That is,

$$u = v = 0 \qquad (13a)$$

$$T_w = \text{Constant} \qquad (13b)$$

The remaining boundaries are permeable. Since these boundaries are artificial (constructed for convenience of solution of physical problem), some special attention is warranted.

To provide guidelines for suitable boundary conditions for the permeable boundaries, a method based upon reference-plane characteristic theory (ref. 19) is applied to the transformed governing flow equations. In this approach, which is used by Cline (ref. 20) and Thomas (ref. 18), the convection terms with cross derivatives (i.e., for the inflow boundary in the present case, $\partial/\partial y$ is a cross-derivative operator) and the viscous and heat-conduction terms are treated as forcing functions. Thus, the hyperbolic-parabolic system of governing partial differential equations is effectively reduced to a hyperbolic quasi-one-dimensional system. The method of characteristics is applied to this new system of equations with two independent variables, namely, one spatial variable (either x or y) and time t. Moreover, the characteristics and corresponding compatibility equations associated with the hyperbolic system are readily obtained. (See ref. 20.) The number of boundary conditions necessary for a given boundary, which depends on the number of compatibility relations valid on the characteristic curves that cross the boundary and enter the physical flow region of interest, is determined (ref. 21). The flow quantities that may be set at a boundary can be deduced from examining the compatibility equations.

The quantities specified at the inflow, outflow, and upper boundaries are discussed in the next three subsections. (See fig. 3.)

Inflow boundary.- If the flow is supersonic ($u > a$), there are four compatibility equations for the three ingoing characteristics (two Mach lines and a path line). Therefore, all dependent flow variables may be specified. For subsonic flow ($u < a$), there are three compatibility relations associated with two ingoing characteristic curves (one Mach line and a path line). Although, in general, ρ, u, and v may be set, the total pressure p_t, total temperature T_t, and flow inclination angle $\bar{\theta}$ are specified here. Thus, the inflow boundary emulates a boundary at which disturbances originating from the interior of the computational domain are absorbed rather than reflected.

Outflow boundary.- If $u > a$, there are no ingoing characteristics into the region of concern. All flow quantities at this boundary can be determined from upstream information. For $u < a$, there is one inward characteristic (Mach line) and one compatibility equation. Because of physical considerations, the static pressure is specified.

Upper boundary.- This boundary is located sufficiently far away from the surface of an afterbody configuration to be considered in the free stream. However, it is a finite distance from the wall boundary. Therefore, in general, it can be of the inflow type, outflow type, or a combination of both. The sign of the r-direction velocity component v at any boundary point determines whether the boundary is treated locally as an inflow type or an outflow type. If v is negative (inflow) or zero, the velocity component in the z-direction u; pressure p, and density ρ are set to their free-stream values. That is,

$$u = 1, \quad \rho = 1, \quad p = p_\infty \tag{14}$$

11

If $v > 0$, only the pressure is specified. This scheme for specifying boundary conditions is used for both subsonic and supersonic free-stream flows.

Numerical Treatment of Boundary Points

At the wall boundary, the density is computed from the continuity equation. The derivatives in the x-direction vanish because of the no-slip condition. The derivatives in the y-direction are replaced with second-order-accurate one-sided differences. Using the density and the specified wall temperature, the pressure is calculated from the ideal gas equation of state.

In the case of a subsonic inflow boundary, a second-order-accurate reference-plane characteristic scheme in conjunction with the appropriate boundary conditions is used to obtain the unknown flow variables. The characteristic compatibility equations, which are derived from the transformed governing equations (for derivation procedure see ref. 19), are as follows:

$$dp - a^2 \, d\rho = \psi_4 \, dt \tag{15a}$$

$$dv = \psi_3 \, dt \tag{15b}$$

$$dp - \rho a \, du = \left(\psi_4 + a^2 \psi_1 - \rho a \psi_2 \right) dt \tag{15c}$$

$$dp + \rho a \, du = \left(\psi_4 + a^2 \psi_1 + \rho a \psi_2 \right) dt \tag{15d}$$

and

$$\left.
\begin{aligned}
\psi_1 &= -\rho y_z u_y - u y_z \rho_y - \rho y_r v_y - v y_r \rho_y - \rho \frac{v}{r} \\[6pt]
\psi_2 &= -u y_z u_y - v y_r u_y - \frac{1}{\rho} y_z p_y + \bar{s}_2 \\[6pt]
\psi_3 &= -u y_z v_y - v y_r v_y - \frac{1}{\rho} y_r p_y + \bar{s}_3 \\[6pt]
\psi_4 &= -u y_z p_y - v y_r p_y + a^2 (u y_z \rho_y + v y_r \rho_y) + \bar{s}_4
\end{aligned}
\right\} \tag{16}$$

where the independent variable subscripts denote partial differentiation. The quantities $\bar{s}_i$ (i = 2,3,4) are viscous source terms. By assuming that the viscous terms associated with transport processes in the x-direction are negligible (a reasonable assumption for high Reynolds number flows) and by noting that the transformation derivatives x_r and y_z are essentially zero, these source terms take the form

$$\bar{s}_2 = \frac{1}{N_{Re}}\left[\frac{1}{\rho}\, y_r\,(\bar{\mu}y_r u_y)_y + \frac{\bar{\mu}}{\rho r}(y_r u_y)\right]$$

$$\bar{s}_3 = \frac{1}{N_{Re}}\left[\frac{1}{\rho}\, y_r\left(\frac{4}{3}\,\bar{\mu}y_r v_y\right)_y + \frac{4}{3}\,\frac{\bar{\mu}}{\rho r}\left(y_r v_y - \frac{v}{r}\right)\right]$$

$$\bar{s}_4 = \frac{(\gamma - 1)}{N_{Re}}\left\{\frac{4}{3}\,\bar{\mu}(y_r v_y)^2 + \bar{\mu}(y_r u_y)^2 + y_r\left[\gamma\left(\frac{\mu}{N_{Pr,m}} + \frac{\varepsilon}{N_{Pr,t}}\right)y_r T_y\right]_y \right.$$
$$\left. + \frac{4}{3}\,\bar{\mu}\left(\frac{v}{r}\right)^2 - \frac{4}{3}\,\bar{\mu}\frac{v}{r}(y_r v_y) + \gamma\left(\frac{\mu}{N_{Pr,m}} + \frac{\varepsilon}{N_{Pr,t}}\right)\frac{1}{r}\,y_r T_y\right\}$$

(17)

where $\bar{\mu} = \mu + \varepsilon$. Equations (15a) and (15b) are valid along the characteristic curve

$$\frac{dx}{dt} = x_z u \tag{18}$$

Compatibility relations (15c) and (15d) are valid along the following characteristics, respectively:

$$\frac{dx}{dt} = x_z(u - a) \tag{19a}$$

$$\frac{dx}{dt} = x_z(u + a) \tag{19b}$$

Since p_t, T_t, and $\bar{\theta}$ are specified at the inflow boundary points, the isentropic relations

$$\frac{T_t}{T} = 1 + \frac{\gamma - 1}{2}\,M^2 \tag{20a}$$

$$\frac{p_t}{p} = \left(1 + \frac{\gamma - 1}{2}\,M^2\right)^{\frac{\gamma}{\gamma - 1}} \tag{20b}$$

and equation (15c) can be used to set up an iterative scheme to determine the inflow Mach number distribution and, therefore, the dependent flow quantities. The procedures required to numerically solve the compatibility equation are discussed by Cline (ref. 20).

The characteristic formulation used for the inflow boundary is also employed in the computation of unspecified flow properties at the outflow boundary when the flow is subsonic. Since only the static pressure is given at outflow points, the density ρ, r-component of velocity v, and z-component

13

of velocity u are calculated along the two outgoing characteristics with compatibility equations (15a), (15b), and (15d), respectively. When the outflow is supersonic, all flow quantities are determined with zero-order extrapolation. That is,

$$\frac{\partial U^*}{\partial x} = 0 \tag{21}$$

where

$$U^* = \begin{bmatrix} \rho \\ u \\ v \\ T \end{bmatrix}$$

For subsonic and supersonic free-stream flows, the boundary conditions at the upper boundary are supplemented with appropriate characteristic equations in order to determine all flow properties. The compatibility relations, which are derived in the same manner as those for the inflow and outflow boundaries, are as follows:

$$dp - a^2 \, d\rho = \psi_4 \, dt \tag{22a}$$

$$y_r \, du - y_z \, dv = (y_r\psi_2 - y_z\psi_3) \, dt \tag{22b}$$

$$dp - \rho y_z \frac{a}{\alpha} \, du - \rho y_r \frac{a}{\alpha} \, dv = \left(a^2\psi_1 - \rho y_z \frac{a}{\alpha} \psi_2 - \rho y_r \frac{a}{\alpha} \psi_3 + \psi_4 \right) dt \tag{22c}$$

$$dp + \rho y_z \frac{a}{\alpha} \, du + \rho y_r \frac{a}{\alpha} \, dv = \left(a^2\psi_1 + \rho y_z \frac{a}{\alpha} \psi_2 + \rho y_r \frac{a}{\alpha} \psi_3 + \psi_4 \right) dt \tag{22d}$$

and

$$\left.\begin{aligned} \alpha &= \left(y_z{}^2 + y_r{}^2 \right)^{1/2} \\[4pt] \psi_1 &= -\rho x_z u_x - u x_z \rho_x - \rho \frac{v}{r} \\[4pt] \psi_2 &= -u x_z u_x - \frac{1}{\rho} x_z p_x + \bar{s}_2 \\[4pt] \psi_3 &= -u x_z v_x + \bar{s}_3 \\[4pt] \psi_4 &= -u x_z p_x + a^2 u x_z \rho_x \end{aligned}\right\} \tag{23}$$

14

Since the flow at this boundary is essentially inviscid, the viscous source terms $\bar{s}_i$ are taken to be zero. The characteristic curve associated with equations (22a) and (22b) is

$$\frac{dy}{dt} = uy_z + vy_r \tag{24}$$

and the characteristic curves corresponding to equations (22c) and (22d) are, respectively,

$$\frac{dy}{dt} = uy_z + vy_r - \alpha a \tag{25a}$$

$$\frac{dy}{dt} = uy_z + vy_r + \alpha a \tag{25b}$$

At inflow points, v is calculated with equation (22d), and the boundary conditions $u = 1$, $\rho = 1$, and $p = p_\infty$ are imposed. Since only p is specified at outflow points, ρ, u, and v are computed from equations (22a), (22b), and (22d).

Inflow Profiles and Initial Conditions

As discussed previously, certain flow properties are required at the inflow boundary of the Navier-Stokes solution domain. Inviscid flow and boundary-layer solution techniques are employed to compute the necessary inflow profiles. The procedures used herein are described for the flow over the axisymmetric body illustrated in figure 1. If the flow is supersonic ($M_\infty > 1$), the inviscid pressure distribution on the surface is calculated from the tip of the conical nose to a location upstream of the beginning of the boattail with a method of characteristics scheme. Then the turbulent boundary-layer equations with a two-layer eddy-viscosity model are solved with the method of Price and Harris (ref. 22). In the case of subsonic ($M_\infty < 1$) flow, the inviscid pressure field is determined by solving the full transonic potential flow equation with the relaxation procedure of South and Jameson (ref. 23). Because of the elliptic character of the flow field, the flow over the entire configuration must be considered. An afterbody with a boattail on which the flow does not separate is used in the inviscid calculation. The resulting inviscid flow field in the vicinity of the inflow boundary is considered a reasonable approximation to the one corresponding to other boattail geometries. A boundary-layer solution is obtained up to a specified position upstream of the start of the boattail. These profiles are interpolated onto the Navier-Stokes grid.

An initial solution for the finite-difference calculations is obtained by extending the inflow profiles over the entire solution domain. For subsonic flow, this crude starting solution is used only if there are no previous results for a configuration similar to the one being computed.

Numerical Solution of Flow Equations

Finite-difference scheme.- The explicit, predictor-corrector finite-difference scheme of MacCormack (ref. 12) is used to integrate the governing flow equations in time to obtain a steady-state solution. This numerical algorithm is second-order accurate in both time and space. When this scheme is applied to equation (1a), the two steps have the following form:

Predictor step

$$
\overline{U_{i,j}^{n+1}} = U_{i,j}^n - (x_z)_{i,j} \frac{\Delta t}{\Delta x}\left(F_{i+1,j}^n - F_{i,j}^n\right)
$$

$$
- (x_r)_{i,j} \frac{\Delta t}{\Delta x}\left(G_{i+1,j}^n - G_{i,j}^n\right) - (y_z)_{i,j} \frac{\Delta t}{\Delta y}\left(F_{i,j+1}^n - F_{i,j}^n\right)
$$

$$
- (y_r)_{i,j} \frac{\Delta t}{\Delta y}\left(G_{i,j+1}^n - G_{i,j}^n\right) - \Delta t\, H_{i,j}^n \tag{26}
$$

Corrector step

$$
U_{i,j}^{n+1} = \frac{1}{2}\left[\overline{U_{i,j}^{n+1}} + U_{i,j}^n - (x_z)_{i,j} \frac{\Delta t}{\Delta x}\left(\overline{F_{i,j}^{n+1}} - \overline{F_{i-i,j}^{n+1}}\right)\right.
$$

$$
- (x_r)_{i,j} \frac{\Delta t}{\Delta x}\left(\overline{G_{i,j}^{n+1}} - \overline{G_{i-1,j}^{n+1}}\right) - (y_z)_{i,j} \frac{\Delta t}{\Delta y}\left(\overline{F_{i,j}^{n+1}} - \overline{F_{i,j-1}^{n+1}}\right)
$$

$$
\left. - (y_r)_{i,j} \frac{\Delta t}{\Delta y}\left(\overline{G_{i,j}^{n+1}} - \overline{G_{i,j-1}^{n+1}}\right) - \Delta t\, \overline{H_{i,j}^{n+1}}\right] \tag{27}
$$

where the subscripts i and j are node indices, and the superscript refers to the time level ($t = n\,\Delta t$). The $\partial F/\partial x$, $\partial G/\partial x$, $\partial F/\partial y$, and $\partial G/\partial y$ terms are approximated by forward differences in the predictor step and by backward differences in the corrector step. The derivatives in the viscous and heat conduction terms are approximated with backward differences in the predictor step and forward differences in the corrector step. In all computations the transformation derivatives are replaced with central differences.

Numerical damping.- In order to suppress point-to-point postshock oscillations that may occur in supersonic calculations, a fourth-order numerical damping procedure (ref. 7) is incorporated. The predictor-corrector form for this scheme can be given by:

16

Predictor step

$$S_{i,j}^n = C_x \frac{\left| p_{i+1,j}^n - 2p_{i,j}^n + p_{i-1,j}^n \right|}{\left(p_{i+1,j}^n + 2p_{i,j}^n + p_{i-1,j}^n \right)} \left(U_{i+1,j}^n - 2U_{i,j}^n + U_{i-1,j}^n \right)$$

$$+ C_y \frac{\left| p_{i,j+1}^n - 2p_{i,j}^n + p_{i,j-1}^n \right|}{\left(p_{i,j+1}^n + 2p_{i,j}^n + p_{i,j-1}^n \right)} \left(U_{i,j+1}^n - 2U_{i,j}^n + U_{i,j-1}^n \right) \tag{28}$$

Corrector step

$$S_{i,j}^{\overline{n+1}} = C_x \frac{\left| p_{i+1,j}^{\overline{n+1}} - 2p_{i,j}^{\overline{n+1}} + p_{i-1,j}^{\overline{n+1}} \right|}{\left(p_{i+1,j}^{\overline{n+1}} + 2p_{i,j}^{\overline{n+1}} + p_{i-1,j}^{\overline{n+1}} \right)} \left(U_{i+1,j}^{\overline{n+1}} - 2U_{i,j}^{\overline{n+1}} + U_{i-1,j}^{\overline{n+1}} \right)$$

$$+ C_y \frac{\left| p_{i,j+1}^{\overline{n+1}} - 2p_{i,j}^{\overline{n+1}} + p_{i,j-1}^{\overline{n+1}} \right|}{\left(p_{i,j+1}^{\overline{n+1}} + 2p_{i,j}^{\overline{n+1}} + p_{i,j-1}^{\overline{n+1}} \right)} \left(U_{i,j+1}^{\overline{n+1}} - 2U_{i,j}^{\overline{n+1}} + U_{i,j-1}^{\overline{n+1}} \right) \tag{29}$$

The terms in equations (28) and (29) are appended to the right-hand side of equations (26) and (27), respectively. Since these terms are fourth-order, they do not compromise the second-order accuracy of the solution. The coefficients C_x and C_y are used to control the amount of damping that is included in a calculation. Care must be exercised to keep these coefficients sufficiently small $\left(\text{in the current work } 0 \leqq (C_x, C_y) \leqq 0.1 \right)$ so that shocks present in the flow field are smeared over the minimum number of grid points possible.

Another form of damping is sometimes necessary for the time-dependent calculations. When the initial solution represents a considerable departure from the steady-state solution, large disturbances are present in the solution domain. The damping associated with the physical viscosity and numerical truncation error is not always adequate to suppress these large initial disturbances. Because of upstream feeding this possibility is strongest when the flow is subsonic. To help remove these large disturbances the solution at each grid point for the first 200 to 400 complete time steps is replaced with the average of the solutions at the four neighboring grid points. The unpublished work of M. C. Cline of Los Alamos Scientific Laboratory shows that this filtering process can also have a significant beneficial effect on the convergence rate.

<u>Numerical stability</u>.- The allowable time step for the MacCormack scheme in the time-marching process is dictated by the Courant-Friedrichs-Lewy (CFL) condition. This criterion can be given by

$$\Delta t = \frac{c}{\dfrac{|v|}{\Delta r} + \dfrac{|u|}{\Delta z} + a\sqrt{\dfrac{1}{(\Delta r)^2} + \dfrac{1}{(\Delta z)^2}}} \tag{30}$$

where a is the speed of sound and c is a specified constant.

<u>Computational efficiency</u>.- The overall computational efficiency is enhanced in two basic ways. First, the numerical procedure is programmed on a vector processor (CYBER 203). Since the algorithm is explicit, it is amenable to complete vectorization (ref. 24). Second, a grid subcycling process is employed in the numerical integration scheme to relax the effect of the time-step requirement, which is very restrictive because of the fine-mesh spacing necessary to resolve the turbulent boundary layer. This subcycling process is based upon the time-step doubling procedure of Holst (ref. 7). The first grid points in the radial direction at which the local allowable time step is greater than or equal to $n_1 \Delta t_{min}$, $2n_1 \Delta t_{min}$, $4n_1 \Delta t_{min}$, $8n_1 \Delta t_{min}$, . . ., are designated time increment points (TIP). The integer $n_1 \geq 2$, and Δt_{min} is the time step corresponding to the minimum radial grid spacing. At each TIP the Δt is increased by a factor of 2 over the value at the previous TIP. To illustrate the subcycling scheme consider the case where the solution in the y-direction at a given x-location is advanced $8 \Delta t_{min}$. Assume that only three TIP's exist (see fig. 4). In the initial step the flow equations are integrated from the wall boundary to the grid point preceding the first TIP. Then, starting at the surface again, they are integrated to the grid point before the second TIP; during this calculation Δt is switched from Δt_{min} to $2 \Delta t_{min}$ at the first TIP. All points below the second TIP are then at time $t = 2 \Delta t_{min}$. On the third integration pass, the point preceding the first TIP is the stopping point. On the fourth pass, integration is continued until the point before the third TIP is reached, and the solution is then at $t = 4 \Delta t_{min}$ at all grid points below the third TIP. The time step is switched from Δt_{min} to $2 \Delta t_{min}$ at the first TIP and from $2 \Delta t_{min}$ to $4 \Delta t_{min}$ at the second TIP. When the subcycling process is completed, the solution at all mesh points is at the same time level, which is $8 \Delta t_{min}$ for this example. Holst reported that with $n_1 = 2$ an explicit code (MacCormack algorithm) with subcycling was about 2.5 to 4 times faster than the same code without subcycling. The speedup depends upon the minimum value of the radial grid spacing and the value of n_1.

In all calculations of this report, the numerical time integration is continued until the maximum change in surface pressure for one complete time step (solution at all grid points at the same time level) is less than 0.2 percent. With this criterion the supersonic solutions required about 5 central processing unit (CPU) minutes on the CYBER 203 computer. When the inflow profiles of the primitive flow variables (ρ, u, v, T) are extended over the solution domain,

convergence for the subsonic computations takes approximately 2.5 CPU hours. This substantial increase in computing time is primarily due to the elliptic character of the inviscid flow field as steady state is approached. Moreover, low-frequency errors in the solution damp out very slowly. If a converged sub-sonic result is used as an initial solution for another afterbody flow (i.e., includes a different boattail), convergence can be achieved in about 1.6 CPU hours.

Turbulence Modeling

In the present application the algebraic eddy-viscosity models of Cebeci and Smith (ref. 13) and Baldwin and Lomax (ref. 14) are implemented, and the results obtained with each model are compared. Each model includes two layers, and thus the turbulence is modeled with two length scales. That is,

$$\varepsilon = \begin{cases} \varepsilon_i & \text{if } \bar{y} \leqq \bar{y}_c \\ \\ \varepsilon_o & \text{if } \bar{y} > \bar{y}_c \end{cases} \tag{31}$$

where $\bar{y}$ is the normal distance from the wall and $\bar{y}_c$ is the smallest value of $\bar{y}$ at which the inner and outer values of ε are equal. For separated flows these basic models are modified with a relaxation formula to account for upstream history effects on the turbulence.

Cebeci-Smith model.- The Cebeci-Smith (C-S) model represents the eddy viscosity in the inner layer with

$$\varepsilon_i = \rho \ell_1^2 \left| \frac{\partial u}{\partial y} \right| N_{Re} \tag{32a}$$

and

$$\ell_1 = K\bar{y}D \tag{32b}$$

where Von Karman's constant $K = 0.4$, and the Van Driest damping factor is as follows:

$$D = 1 - \exp(-\bar{y}^+/A^+) \tag{32c}$$

The dimensionless distance

$$\bar{y}^+ = \frac{\rho_w u_\tau \bar{y} N_{Re}}{\mu_w} \tag{32d}$$

19

$$u_\tau = \sqrt{\frac{|\tau_w|}{\rho_w}} \tag{32e}$$

and

$$A^+ = 26 \tag{32f}$$

In all calculations the normal distance is replaced with the radial distance. The eddy viscosity in the outer layer is given by

$$\varepsilon_o = 0.0168\rho u_e \delta_i^* N_{Re} F_{Kleb}(\bar{y}) \tag{33a}$$

where u_e is the boundary-layer edge velocity, δ_i^* is the incompressible displacement thickness

$$\delta_i^* = \int_{\bar{y}_o}^{\bar{y}_e} \left(1 - \frac{u}{u_e}\right) d\bar{y} \tag{33b}$$

and $F_{Kleb}(\bar{y})$ is the Klebanoff intermittency function

$$F_{Kleb}(\bar{y}) = \left[1 + 5.5\left(\frac{C_{Kleb}\bar{y}}{\bar{y}^*}\right)^6\right]^{-1} \tag{33c}$$

The constant $C_{Kleb} = 1.0$ and $\bar{y}^* = \delta$. The distance $\bar{y}_o$ is measured from the surface to the point of zero velocity so as to exclude the separated flow region. In this way a large reverse flow region does not cause unrealistic values of ε_o. Usually, the edge of the boundary layer $\bar{y}_e$ is defined as the point at which the u-component of the velocity is 99.5 percent of the free-stream value. However, this edge criterion can result in a value of $\bar{y}_e$ that is far beyond the edge of the boundary layer when the velocity profile is distorted because of the presence of a shock in the flow field or a sufficiently strong viscous-inviscid interaction. This can result in a displacement thickness that is as much as 2 times larger than the actual value (ref. 25). With this larger value of the outer-layer length scale, the mixing in the outer region of the turbulent boundary layer is larger. For the transonic flows being considered in this work, a total-pressure criterion is used to determine the edge of the viscous layer. Moreover, the point at which the local total pressure is $0.995p_{t,\infty}$ is defined as $\bar{y}_e$. Since a p_t profile is less sensitive to the presence of a transonic shock wave than the velocity profile, the true edge of the boundary layer should be more accurately determined.

Baldwin-Lomax model.- The Baldwin-Lomax (B-L) model represents the inner eddy viscosity with

$$\varepsilon_i = \rho \ell_1^2 |\omega| N_{Re} \tag{34a}$$

where $|\omega|$ is the magnitude of the vorticity vector. In axisymmetric flow

$$|\omega| = \left| \frac{\partial u}{\partial r} - \frac{\partial v}{\partial z} \right| \tag{34b}$$

The form for the outer eddy viscosity is

$$\varepsilon_o = 0.0168 C_{cp} \rho N_{Re} F_{wake} F_{Kleb}(\bar{y}) \tag{35a}$$

where

$$F_{wake} = \bar{y}_{max} F_{max} \tag{35b}$$

The quantity $\bar{y}_{max}$ is the location at which the maximum (F_{max}) of $F(\bar{y})$ occurs, and

$$F(\bar{y}) = \bar{y} |\omega| D \tag{35c}$$

In equation (35a) the constants are

$$C_{cp} = 1.6$$

$$C_{Kleb} = 0.3 \tag{35d}$$

and

$$\bar{y}^* = \bar{y}_{max} \tag{35e}$$

Relaxation models.- Although the turbulence in a flow does not respond immediately to a sudden change in the mean flow (i.e., a switch from zero or favorable pressure gradient to adverse pressure gradient), it does retain memory of the change. A relaxation or lag model attempts to take into account the memory of the turbulence. The relaxation models that include the simple alge-braic models are of the following types: global and local. In a typical global model, the value of the eddy viscosity at a point on a streamline (or a constant body-fitted coordinate line) and downstream of some disturbance depends on the eddy viscosity at a point, e.g. z_I, upstream of the change in the flow character and located on the same streamline. This dependence decreases as the distance from z_I increases, and eventually the viscosity takes on an equilibrium value. A local lag model allows the turbulent viscosity at a point in the flow field to depend only on the viscosity at the preceding point (i.e., Δz upstream) on a

streamline. A number of investigations (refs. 7, 15, 25, and 26) have shown that a global relaxation model yields better surface-pressure predictions than the basic algebraic model when the free-stream flow is supersonic and flow separation occurs. In reference 27 Deiwert employed a local relaxation model to compute separated transonic flow over a circular-arc airfoil. The surface-pressure results obtained with this model were in better agreement with experimental data than those calculated without relaxation. However, the pressure variation in the separated region was not improved.

In the present work the global relaxation model suggested by Shang and Hankey (ref. 15) is used. With this model the relaxed eddy viscosity is evaluated from

$$\varepsilon_R(z) = \varepsilon_I + (\varepsilon - \varepsilon_I)\left\{1 - \exp\left[(z_I - z)/\lambda\right]\right\} \tag{36}$$

where ε_I is the value of the eddy viscosity at location z_I (the axial coordinate at the start of relaxation), ε is the local eddy viscosity calculated with either the Cebeci-Smith or Baldwin-Lomax model, and λ is a relaxation length parameter specified at the beginning of a calculation. In the separated subsonic flows considered in this report, z_I is placed at the point of minimum pressure, which occurs on the shoulder of a boattail and upstream of separation. The minimum-pressure location is determined with $\lambda = 0$ (no relaxation), and relaxation is initiated in the calculation after this determination. For the supersonic cases z_I is located at about δ_s, boundary-layer thickness at separation, upstream of the separation point (determined with $\lambda = 0$). This location nearly corresponds to the point of minimum pressure.

RESULTS AND DISCUSSION

In this section results from the solutions for transonic flow over three axisymmetric afterbodies, each consisting of a cylinder, circular-arc boattail, and cylindrical plume simulator, are presented. Calculations were performed for free-stream Mach numbers of 0.8 and 1.3 for each configuration, and the flows considered ranged from fully attached to highly separated. The attached or nearly attached flow cases are used to establish artificial boundary locations and finite-difference grid requirements. For the subsonic problems the following conditions were imposed:

$$p_{t,\infty} = 1.70 \qquad T_t = 3.15 \qquad T_w = 3.11 \qquad N_{Re} = 2.23 \times 10^6$$

$$\hat{p}_{ref} = 58.74 \text{ kPa} \qquad \hat{T}_{ref} = 105.2 \text{ K}$$

In the supersonic cases the prescribed conditions were:

$$p_{t,\infty} = 1.17 \qquad T_{t,\infty} = 1.41 \qquad T_w = 1.30 \qquad N_{Re} = 1.03 \times 10^6$$

$$\hat{p}_{ref} = 87.09 \text{ kPa} \qquad \hat{T}_{ref} = 240.5 \text{ K}$$

The numerical predictions obtained by solving the time-averaged Navier-Stokes equations are compared with the experimental data of Putnam and Abeyounis (ref. 1) and Reubush (ref. 11). The parameters describing the boattails are given in figure 5. The ratio of boattail length to boattail-exit diameter ℓ varies from 3.5 to 1.6, and the corresponding chord boattail angles β_c vary from 7.9° to 17°.

Subsonic Solutions

Attached flow case.- A solution was obtained for flow over afterbody configuration 3 with $M_\infty = 0.8$. The finite-difference grid consisted of 51 points in the axial direction (22 points in boattail region) and 61 points in the radial direction (about half the points in the viscous layer). The first mesh point off the afterbody was located at a distance of 0.001$\hat{d}_e$ from the surface, and the y^+ value for this point was about 19. Therefore, this point was in the inner part of the buffer region (transitional region between laminar sublayer and inner turbulent layer) of the turbulent boundary layer. The inflow boundary of the physical space of concern (see fig. 1) was placed approximately 3.4$\hat{d}_e$ ahead of the beginning of the boattail. This was done to ensure that the flow would have sufficient distance in which to recover from any mismatch between the approximate solution, which provided the necessary quantities for the inflow boundary conditions, and the Navier-Stokes solution. The outflow boundary was situated far enough downstream (5$\hat{d}_e$ from the junction of the boattail and simulator) for the flow to become cylindrical in character and have minimal influence on the boattail region. The upper boundary was located at $r = 4$.

The variation of the calculated surface-pressure coefficient C_p with the nondimensional axial distance z for the physical domain described in the preceding paragraph is compared with experimental data in figure 6. The prediction of the recompression of the boattail flow is in very good agreement with the measured data. The computed C_p values on the plume simulator also compare very well with experiment. However, the pressures in the expansion part of the boattail flow are overpredicted. This indicates that the inviscid pressures imposed on the boundary layer in the expansion region are too high, and the velocities at the edge of the viscous layer are too low.

The overprediction of pressures on the shoulder of the boattail requires further attention. In the calculation the upper boundary was an inflow boundary, which means that the u-component of velocity is specified and takes on the

free-stream value. Therefore, if the upper boundary were too close to the surface, the edge velocities of the boundary layer would be forced to be smaller than they should be.

In order to assess the effect of the upper boundary location, a calculation was performed with the upper boundary moved to $r = 12$. The surface-pressure distribution, which is shown in figure 6, is in excellent agreement with the experimental data. The Cebeci-Smith (C-S) and the Baldwin-Lomax (B-L) turbulence models (to be referred to as baseline models) gave essentially the same results for this problem. In figure 7 the pressure field for the entire flow region is represented in the form of constant contour levels in intervals of 0.02.

The calculated velocity profiles at three axial stations (slightly beyond the start of the boattail, just downstream of the end of the boattail, and almost at the midpoint of the plume simulator) are displayed in figure 8. These profiles are compared with those from a boundary-layer solution (ref. 22) which used the surface afterbody pressures obtained from the Navier-Stokes solution. In the boundary-layer computation the minimum grid spacing in the $\bar{y}$-direction (direction normal to body surface) was about 3.03×10^{-6}, which is more than two orders of magnitude smaller than the value for the Navier-Stokes grid. There were 200 to 300 points, depending upon δ, in the viscous layer. These solutions are in good agreement. Thus, good boundary-layer definition is indicated for the Navier-Stokes result.

Separated flow cases.- In figure 9 predicted surface pressures are compared with the experimental data for afterbody configuration 2 at a free-stream Mach number of 0.8. The pressures calculated with the two baseline turbulence models exhibit only small quantitative differences. With these models the expansion on the boattail is captured; however, the C_p values between the minimum pressure location and separation are too low. There are large differences between predictions and experiment in the reverse flow region, and there is early reattachment of the separated flow. Downstream of the positive experimental C_p peak value, the predictions are good. Finally, using either of the baseline turbulence models, the computed separation location agrees very well with the value obtained from oil-flow studies (ref. 28).

For the implementation of the C-S and B-L turbulence models with relaxation, hereafter designated as R(C-S) and R(B-L), the point at which relaxation is initiated z_I and the relaxation-length scale λ must be specified. As mentioned previously, the delayed response of the turbulence to a rather abrupt application of an adverse pressure gradient is modeled by starting the relaxation at the point of minimum pressure (i.e., just prior to onset of $\partial p/\partial z > 0$). The influence of the quantity λ on the surface-pressure variation for afterbody configuration 2 when the R(C-S) model is employed is shown in figure 10. The lag length scale is varied from zero to infinity. When λ is zero, the R(C-S) model reduces to the equilibrium model (C-S), and when λ is infinity, the eddy viscosity at z_I and $y = $ Constant is maintained in the downstream portion of the flow. The result for $\lambda = 20\delta_I$, where δ_I is the boundary-layer thickness at the beginning of the relaxation, appears to exhibit the best overall agreement with the experimental data.

In figure 11 the pressure distributions calculated with the two relaxation turbulence models are compared. For each case λ equals $20\delta_I$. The results obtained with these models are in good agreement with laboratory data upstream and downstream of the separation region. The solution using the R(B-L) model agrees a little better with the experiment at the pressure plateau than the solution using the R(C-S) model. However, both results slightly underpredict the pressure peak in the vicinity of reattachment. This seems to suggest that reattachment occurs too soon. Nevertheless, these solutions represent a substantial improvement over those determined with the baseline models.

In order to understand the effects of relaxation, the viscosity variations in the radial direction at three axial stations are considered in figure 12. These distributions were computed with $\lambda = 0$ and $\lambda = 20\delta_I$ using the R(C-S) model. They show that there is a decrease in eddy viscosity in the outer turbulent layer of the viscous region when relaxation is used. This means that there is a decrease in turbulent mixing and, therefore, suggests that less streamwise momentum is being transported from the outer part into the inner part of the boundary layer. Such behavior could account for the increased longitudinal extent of the separation bubble when a relaxation model is applied. (See figs. 9 and 11.) The lower values of eddy viscosity also indicate smaller turbulent shearing stresses in the outer portion of the viscous layer. This would be a contributing factor in the reduction of surface pressures in the pressure plateau.

The final case investigated with $M_\infty = 0.8$ was flow over afterbody configuration 1, which has the steepest boattail chord angle (about 17°) considered. Surface pressures determined for this case are compared with measurements in figure 13. The qualitative and quantitative trends exhibited by the predictions with the baseline turbulence models are essentially the same as those described for configuration 2. The wall-pressure solution obtained using the R(C-S) model and $\lambda = 20\delta_I$ shows a pressure plateau region, but the pressures are too high. This is probably because separation is predicted too late (nearly $0.3\hat{d}_e$ beyond the experimental value). Since the separation location computed with the C-S model is almost the same, there appears to be a deficiency with the C-S model for this particular flow. The minimum experimental pressure is slightly overpredicted, but the recompression is predicted very well. The agreement is fairly good downstream of reattachment. The complete pressure field for this solution is presented in figure 14. Also, in figure 15 the u-velocity profiles at four axial stations are shown.

The wall C_p values determined with the R(B-L) model and $\lambda = 20\delta_I$ are also given in figure 13. These values agree very poorly with the laboratory data. Since the prediction for configuration 2 is fairly good, the following question arises: Why does the R(B-L) model perform so poorly for the configuration 1 case? To investigate this question some of the properties of the B-L model were considered. For example, with the B-L model the eddy viscosity in the outer layer of a turbulent boundary layer is proportional to the product $F_{max}\bar{y}_{max}$, where $\bar{y}_{max}$ is the $\bar{y}$ location at which the maximum of $F(\bar{y})$ occurs. The function $F(\bar{y})$ depends on the magnitude of the vorticity. (See section entitled "Turbulence Modeling.") The variation of $\bar{y}_{max}$ with z for

configurations 2 and 1 is displayed in figure 16. Note the large drop in $\bar{y}_{max}$ for configuration 1 just downstream of the beginning of the boattail. This drop is caused by an increase in vorticity level in the inner layer of the viscous region. Moreover, the function $F(\bar{y})$ exhibits a double peak rather than the usual single peak. As a result of the drop in $\bar{y}_{max}$, the values of the outer eddy viscosity undergo an abrupt and substantial decrease. From the previous discussion on relaxation, one can see that this decrease in turbulent mixing in conjunction with the subsonic character of the flow would tend to account for the prediction with the R(B-L) model. Furthermore, if a single relaxation length is desired in the application of the R(B-L) model to a given class of subsonic flows, this behavior points to the need for either redefining the outer length scale $\bar{y}_{max}$ or developing a different type of relaxation formula.

An additional calculation was made with the R(B-L) model and with the local outer length scale based upon the position at which the second peak value of $F(\bar{y})$ occurs. In this case the peak of $F(\bar{y})$ was determined by starting at an approximate location for the edge of the boundary layer and searching inward along a line where $z = $ Constant. As shown in figure 17, the resulting pressure distribution, except for minor differences in the separation bubble, is the same as that obtained with the R(C-S) model.

<center>Supersonic Solutions</center>

Nearly attached flow case.- A calculation was done for afterbody configuration 3 when the free-stream Mach number was 1.3. A 41 × 51 grid was used, and there were 19 points in the boattail region. The minimum grid spacing in the radial direction was $0.001\hat{d}_e$. The inflow boundary was located at $2\hat{d}_e$ before the start of the boattail, and the outflow boundary was placed at about $4\hat{d}_e$ beyond the end of the boattail. In this case, an oblique shock impinges on the viscous layer just upstream of the point where the boattail joins the plume simulator. The upper boundary of the physical domain was placed a sufficient distance from the wall boundary so that the shock did not intersect it. Therefore, the boundary conditions at this boundary could be applied in the same manner as in the subsonic case.

Variations of surface-pressure coefficient for the afterbody flow are shown in figure 18. The decrease in pressure during acceleration of the flow over the boattail is in good agreement with the experiment. The minimum boattail pressure occurs much further downstream of the start of the boattail ($\approx 2.6\hat{d}_e$) than it does in the subsonic case. This is certainly a consequence of the lack of upstream feeding in the inviscid flow field. There is an overprediction of the pressure rise associated with the shock; however, the C_p variation beyond the experimental peak value of C_p agrees reasonably well with the data. The result obtained with the B-L turbulence model is generally in agreement with that determined with the C-S model. It does show a small decrease in the peak positive value of C_p. In each solution a very small shock-induced separation region is predicted, and the separation and reattachment points are indicated in figure 18.

Solutions computed using the R(C-S) and R(B-L) models are also presented in figure 18. In both cases λ was assigned a value of $10\delta_I$ (length scale suggested by previously investigated supersonic flows with separation, refs. 7 and 15), and relaxation was initiated at $z \approx 4.98$. There is less pressure rise with these predictions than with those obtained with the baseline models. The longitudinal extent of the reverse flow region is about the same. However, the overall size of this region is a little larger.

Since the streamwise flow-field gradients are large in the vicinity of the boattail and plume-simulator juncture, some additional calculations were performed for configuration 3 with a refined grid in the z-direction at the juncture. A 51 × 51 grid was used, and Δz at the juncture was about 0.016, which is approximately 0.125 of the value in the previous computations. For both baseline turbulence models the refined grid pressure distribution was somewhat smoother in the neighborhood of the juncture. The results with all four turbulence models exhibited about the same pressure variation in the junctional region as those determined with the coarser grid. The surface pressures were slightly higher downstream of $z \approx 7.4$ in the refined grid cases.

In figure 19 the salient features of the supersonic flow field are displayed with a pressure contour plot. The approximate position of the oblique shock is readily discernible. Characteristics of the flow field are also illustrated in the computed u-velocity profiles at four axial stations in figure 20. These characteristics include the inviscid acceleration, which results from the expansion on the boattail, and the viscous-inviscid interactions.

Separated flow cases.- The surface-pressure distributions for afterbody configurations 2 and 1 with $M_\infty = 1.3$ are shown in figures 21 and 22. The pressures corresponding to the inviscid expansion are predicted very well, except near the minimum-pressure location, for all four turbulence models. For both configurations the calculated C_p values using the baseline models exhibit very poor agreement with data beyond the experimental negative peak value of C_p. In the application of the R(C-S) and R(B-L) models, the length scales for relaxation λ were taken to be $5\delta_I$ and $2.5\delta_I$, respectively. The results with the R(C-S) model are in fairly good agreement except in the pressure plateau region. Although there is a plateau in the recirculating region, the computed C_p values are too high. Separation is probably downstream of where it should be. With the R(B-L) model, the initial part of the plateau is nearly reproduced, but the extent of the plateau in the z-direction is underpredicted. Moreover, the start of the pressure rise in the separation bubble occurs too early. Such behavior is principally due to the sharp decrease in the viscosity levels when the flow changes from highly accelerating to highly decelerating. This occurs in the calculation for configuration 2 as well as that for configuration 1 because of the higher streamline curvature with the supersonic flows than with the subsonic flows.

The influence of λ on the pressure variation is shown for configuration 1 in figure 23. The trends displayed in these results calculated with the R(C-S) model are the same as those associated with the R(B-L) model when the relaxation parameter is varied between zero and infinity.

The pressure field for configuration 2 and the Mach number variations for configuration 1 are presented in the contour plots in figures 24 and 25. The prominent features of these flow fields are depicted. For example, the separation and reattachment shocks which coalesce to form a single shock are evident. The combined effect of this lambda-type shock and the viscous-inviscid interaction on the u-velocity profiles for the flow past configuration 1 (computed with the R(C-S) model) is revealed in figure 26. There is a large separation region present in this case. The maximum reverse-flow velocity is about 29 percent of the free-stream velocity, and the maximum radial distance from the surface to the outer boundary of the separation bubble is about $0.1\hat{d}_e$. For the corresponding subsonic case these same quantities are about 13 percent and $0.074\hat{d}_e$. In the configuration 2 computation, the maximum reverse velocity with the R(C-S) model is $0.19u_\infty$ when M_∞ is 1.3, and $0.09u_\infty$ when M_∞ is 0.8.

CONCLUDING REMARKS

The mass-averaged Navier-Stokes equations have been solved for turbulent transonic flows over axisymmetric afterbodies. Although only circular-arc boattails were considered in this paper, the solution procedure has been formulated to treat arbitrary geometries. Boattail-plume simulator surface-pressure distributions have been computed and compared with experimental data. Four algebraic models have been considered for turbulence closure. Very good agreement with experiment was obtained using two-layer eddy-viscosity models for an attached subsonic ($M_\infty = 0.8$) turbulent flow. Although a solution for the same configuration at $M_\infty = 1.3$ overpredicts the pressures in the vicinity of the boattail-plume simulator juncture, the agreement with experiment is generally fairly good.

As expected, the standard equilibrium turbulence models are not adequate in the calculation of moderately to strongly separated flows. They neither account for the influences of pressure gradient nor include upstream history effects. For both subsonic and supersonic cases, the computed surface pressures using the R(C-S) model (relaxation with Cebeci-Smith model) generally show good quantitative agreement with measured data, except in the reverse-flow region. With this model the qualitative behavior in the separation bubble is captured, but the pressures in the separation region are overpredicted.

Some similar results were obtained with the R(B-L) model (relaxation with Baldwin-Lomax model). The dependency of this model on local vorticity can have adverse effects on the flow solution when a simple relaxation formula is used, and the outer length scale in the viscous region is defined in its original manner.

The results of this investigation suggest that an eddy-viscosity model in conjunction with an appropriate form of relaxation may possibly be adequate to simulate the pressure field of a separated boattail flow. However, detailed turbulence measurements of afterbody flow fields are required in order to obtain a satisfactory relaxation formula and to provide calibration and verification of the associated turbulence model.

Langley Research Center
National Aeronautics and Space Administration
Hampton, VA 23665
December 1, 1980

REFERENCES

1. Putnam, Lawrence E.; and Abeyounis, William K.: Experimental and Theoretical Study of Flow Fields Surrounding Boattail Nozzles at Subsonic Speeds. AIAA Paper No. 76-675, July 1976.

2. Cosner, Raymond R.; and Bower, William W.: A Patched Solution of the Transonic Flowfield About an Axisymmetric Boattail. AIAA Paper No. 77-227, Jan. 1977.

3. Yaros, S. F.: Prediction of Pressure Distributions on Axisymmetric Bodies in Transonic Flow. AIAA Paper No. 77-226, Jan. 1977.

4. Wilmoth, R. G.; Dash, S. M.; and Pergament, H. S.: A Numerical Study of Jet Entrainment Effects on the Subsonic Flow Over Nozzle Afterbodies. AIAA Paper 79-0135, Jan. 1979.

5. Wilmoth, Richard G.: Computation of Transonic Boattail Flow With Separation. NASA TP-1070, 1977.

6. Kuhn, G. D.: Calculation of Separated Turbulent Flows on Axisymmetric Afterbodies Including Exhaust Plume Effects. AIAA Paper 79-0303, Jan. 1979.

7. Holst, T. L.: Numerical Solution of Axisymmetric Boattail Fields With Plume Simulators. AIAA Paper 77-224, Jan. 1977.

8. Mikhail, Ameer G.; Hankey, Wilbur L.; and Shang, Joseph S.: Computation of a Supersonic Flow Past an Axisymmetric Nozzle Boattail With Jet Exhaust. AIAA Paper 78-993, July 1978.

9. Jacocks, J. L.: Computation of Axisymmetric Separated Nozzle-Afterbody Flow. AEDC-TR-79-71, U.S. Air Force, Jan. 1980. (Available from DTIC as AD A079 694.)

10. Deiwert, G. S.: Numerical Simulation of Three-Dimensional Boattail Afterbody Flow Fields. AIAA 80-1347, July 1980.

11. Reubush, David E.: Experimental Study of the Effectiveness of Cylindrical Plume Simulators for Predicting Jet-On Boattail Drag at Mach Numbers up to 1.30. NASA TN D-7795, 1974.

12. MacCormack, Robert W.: The Effect of Viscosity in Hypervelocity Impact Cratering. AIAA Paper No. 69-354, Apr.-May 1969.

13. Cebeci, Tuncer; Smith, A. M. O.; and Mosinskis, G.: Calculation of Compressible Adiabatic Turbulent Boundary Layers. AIAA J., vol. 8, no. 11, Nov. 1970, pp. 1974-1982.

14. Baldwin, Barrett; and Lomax, Harvard: Thin-Layer Approximation and Algebraic Model for Separated Turbulent Flows. AIAA Paper 78-257, Jan. 1978.

15. Shang, J. S.; and Hankey, W. L., Jr.: Numerical Solution for Supersonic Turbulent Flow Over a Compression Ramp. AIAA J., vol. 13, no. 10, Oct. 1975, pp. 1368-1374.

16. Rubesin, Morris W.; and Rose, William C.: The Turbulent Mean-Flow, Reynolds-Stress, and Heat-Flux Equations in Mass-Averaged Dependent Variables. NASA TM X-62248, 1973.

17. Thompson, Joe F.; Thames, Frank C.; and Mastin, C. Wayne: Boundary-Fitted Curvilinear Coordinate Systems for Solution of Partial Differential Equations on Fields Containing Any Number of Arbitrary Two-Dimensional Bodies. NASA CR-2729, 1977.

18. Thomas, P. D.: Numerical Method for Predicting Flow Characteristics and Performance of Nonaxisymmetric Nozzles - Theory. NASA CR-3147, 1979.

19. Zucrow, Maurice J.; and Hoffman, Joe D.: Gas Dynamics - Volume II. John Wiley & Sons, c.1977.

20. Cline, Michael C.: VNAP: A Computer Program for Computation of Two-Dimensional, Time-Dependent Compressible, Viscous, Internal Flow. LA-7326, Los Alamos Sci., Lab., Univ. of California, Nov. 1978.

21. Kreiss, Heinz Otto: Initial Boundary Value Problems for Hyperbolic Systems. Commun. Pure & Appl. Math., vol. XXIII, no. 3, May 1970, pp. 277-298.

22. Price, Joseph M.; and Harris, Julius E.: Computer Program for Solving Compressible Nonsimilar-Boundary-Layer Equations for Laminar, Transitional, or Turbulent Flows of a Perfect Gas. NASA TM X-2458, 1972.

23. South, Jerry C., Jr.; and Jameson, Antony: Relaxation Solutions for Inviscid Axisymmetric Transonic Flow Over Blunt or Pointed Bodies. AIAA Computational Fluid Dynamics Conference, July 1973, pp. 8-17.

24. Lambiotte, Jules J., Jr.; and Howser, Lona M.: Vectorization on the STAR Computer of Several Numerical Methods for a Fluid Flow Problem. NASA TN D-7545, 1974.

25. Hung, C. M.; and MacCormack, R. W.: Numerical Simulation of Supersonic and Hypersonic Turbulent Compression Corner Flows Using Relaxation Models. AIAA Paper No. 76-410, July 1976.

26. Shang, J. S.; Hankey, W. L., Jr.; and Law, C. Herbert: Numerical Simulation of Shock Wave - Turbulent Boundary Layer Interaction. AIAA Paper No. 76-95, Jan. 1976.

27. Deiwert, George S.: Computation of Separated Transonic Turbulent Flows. AIAA Paper No. 75-829, June 1975.

28. Abeyounis, William Kelly: Boundary-Layer Separation on Isolated Boattail Nozzles. NASA TP-1226, 1978.
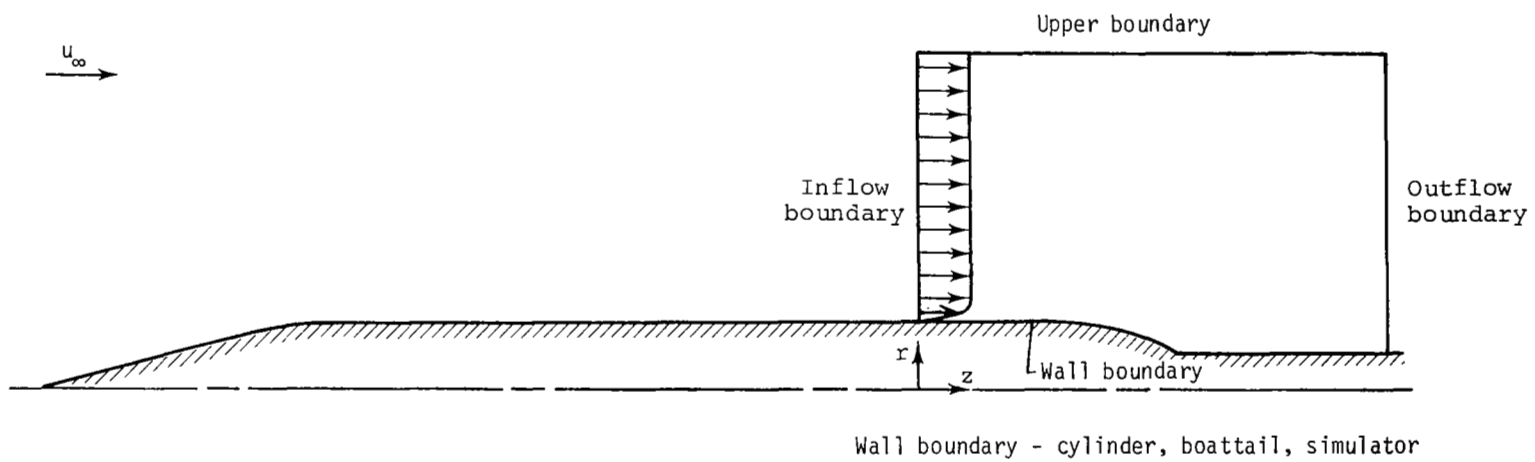
Figure 1.- Navier-Stokes solution region for flow past
cone-cylinder-afterbody configuration.
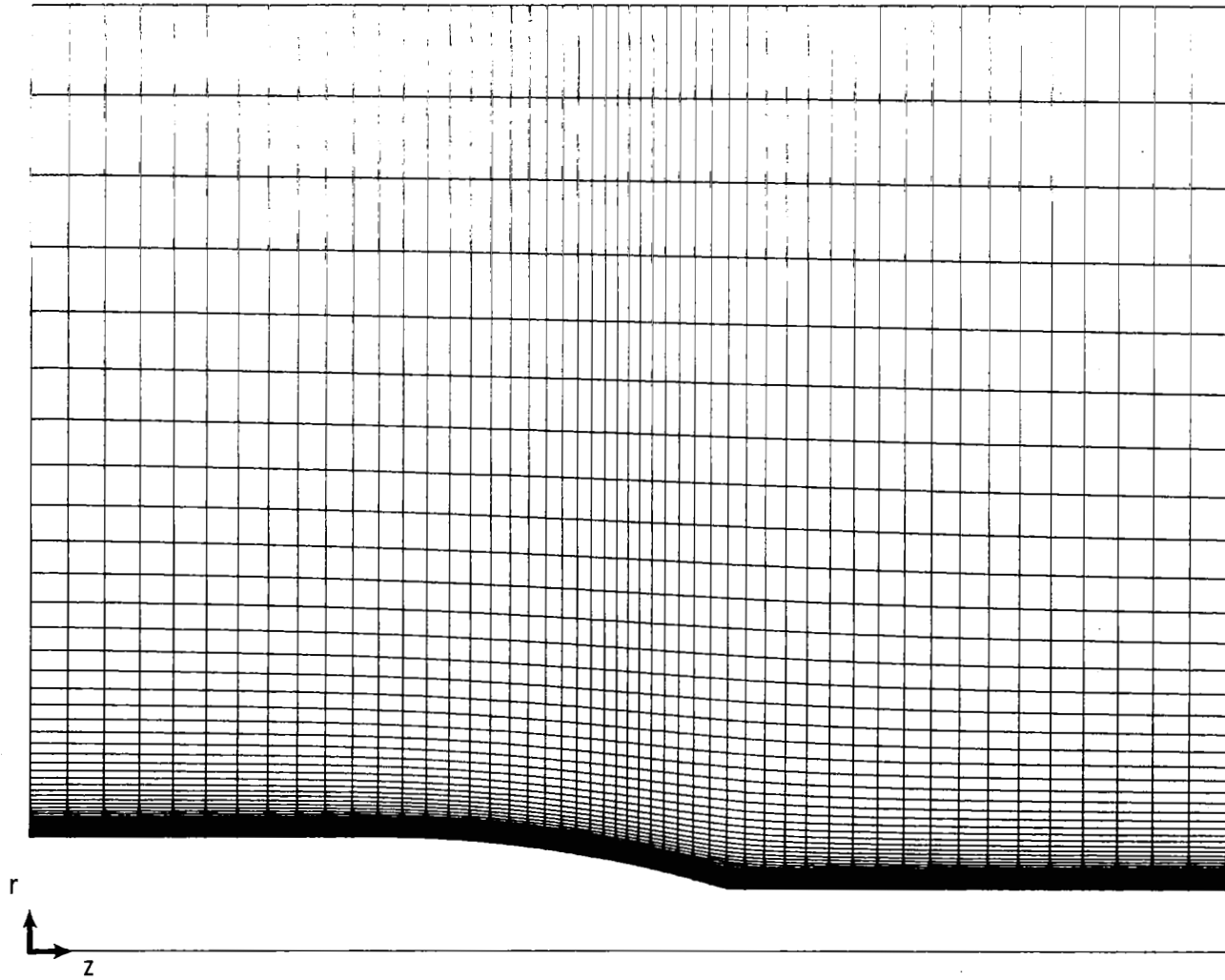
Figure 2.- A typical finite-difference grid in the physical domain.

Subsonic cases

Upper boundary

Inflow - $\rho = 1$, $u = 1$, $p = p_\infty$

Outflow - $p = p_\infty$

Inflow
boundary

p_t, T_t, $\bar{\theta}$
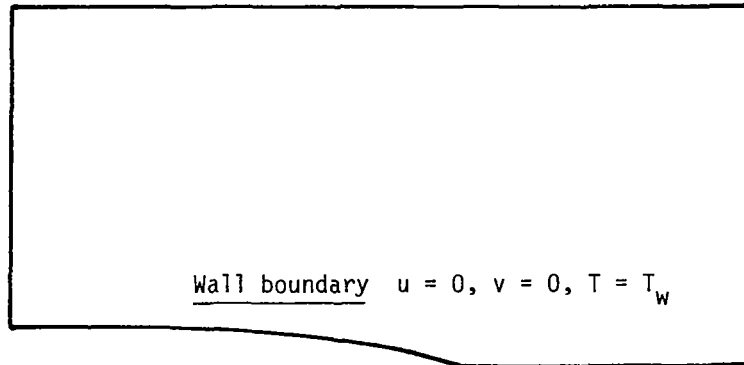
Outflow
boundary

$p = p_\infty$

Wall boundary $u = 0$, $v = 0$, $T = T_w$

Supersonic cases

Upper boundary

Inflow - $\rho = 1$, $u = 1$, $p = p_\infty$

Outflow - $p = p_\infty$

Inflow
boundary

ρ, u, v, T
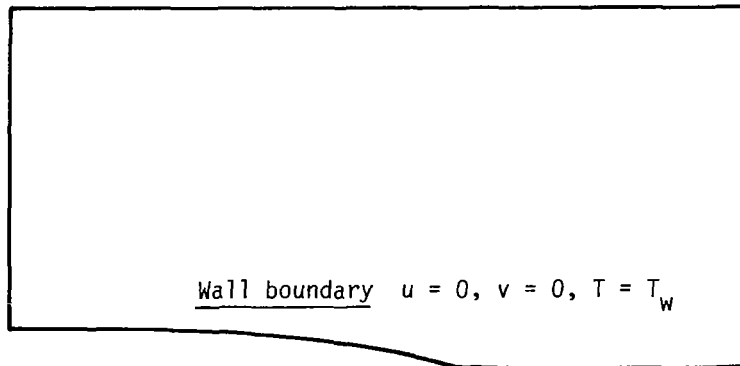
Outflow
boundary

No flow
quantity
specified

Wall boundary $u = 0$, $v = 0$, $T = T_w$

Figure 3.- Flow quantities specified at boundaries of physical domain.

X Grid point

⊗ Grid point at which solution is computed

● Time increment point (TIP)

$$\Delta t_1 = \Delta t_{min}$$
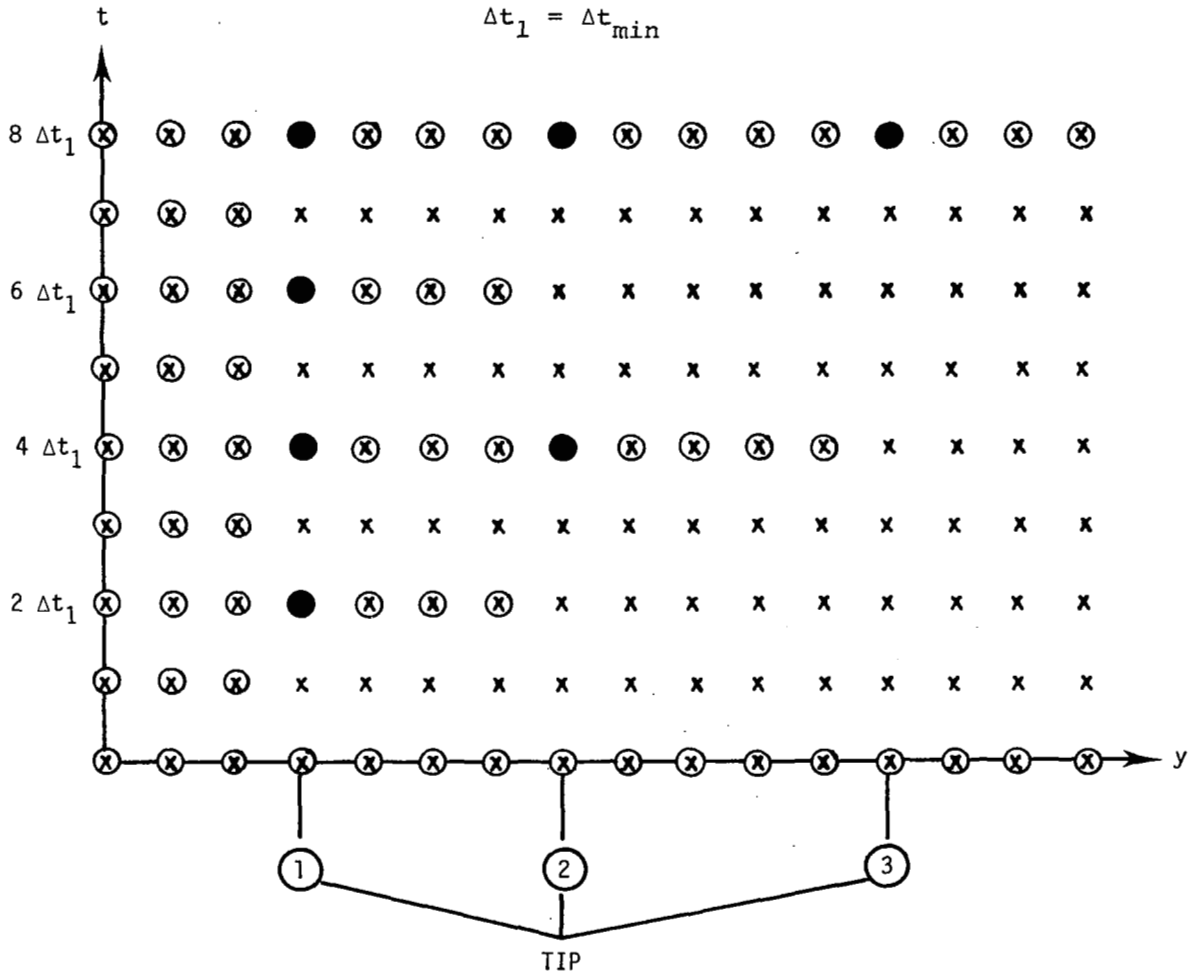
Figure 4.- Grid subcycling procedure.

Figure 5.- Boattail geometric parameters.
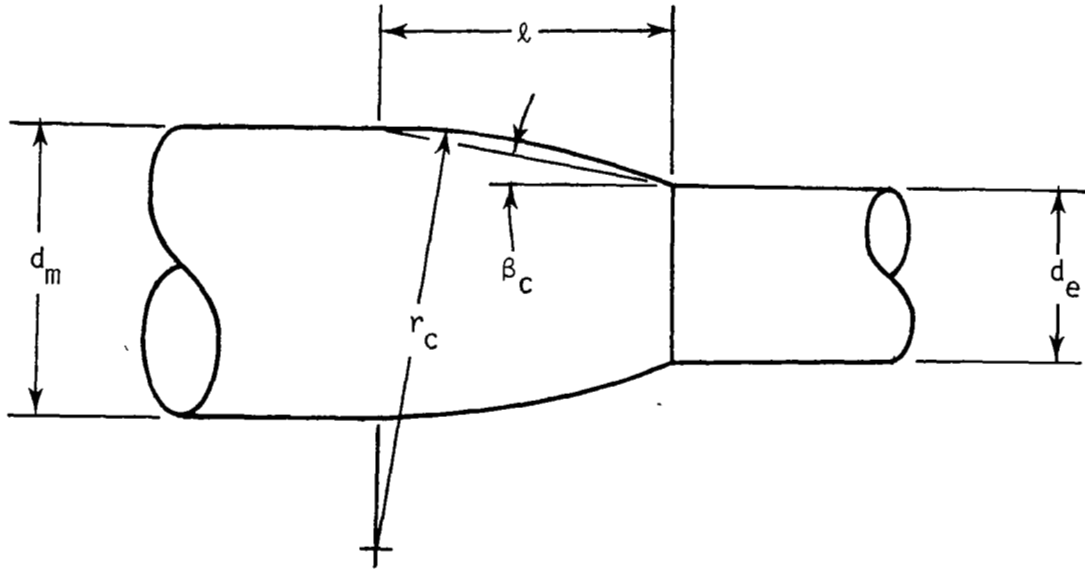
| Configuration	ℓ	d_m	r_c	β_c, deg
3	3.536	2.000	13.000	7.891
2	2.000	2.000	4.326	13.766
1	1.600	2.000	2.858	17.027
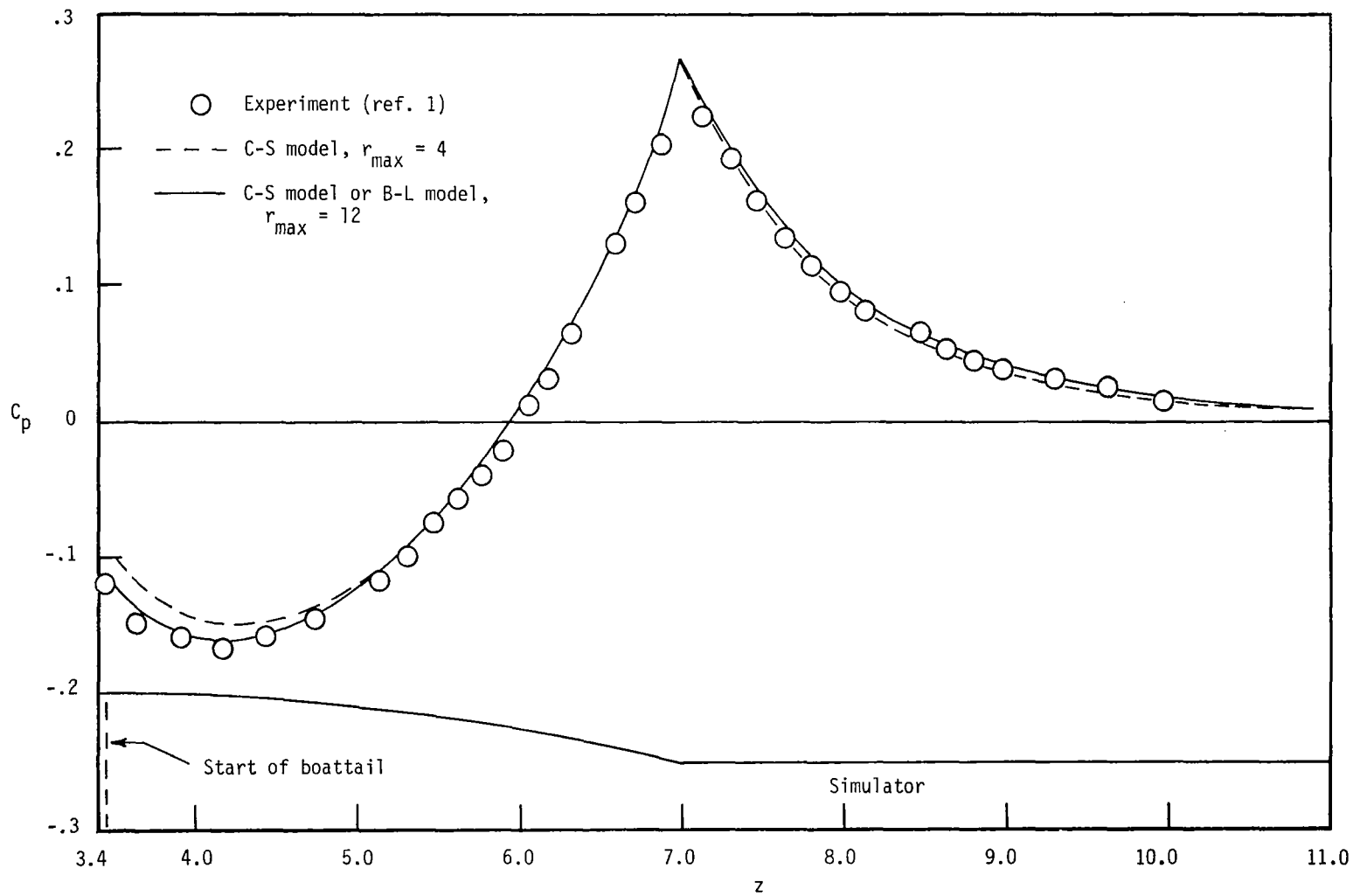
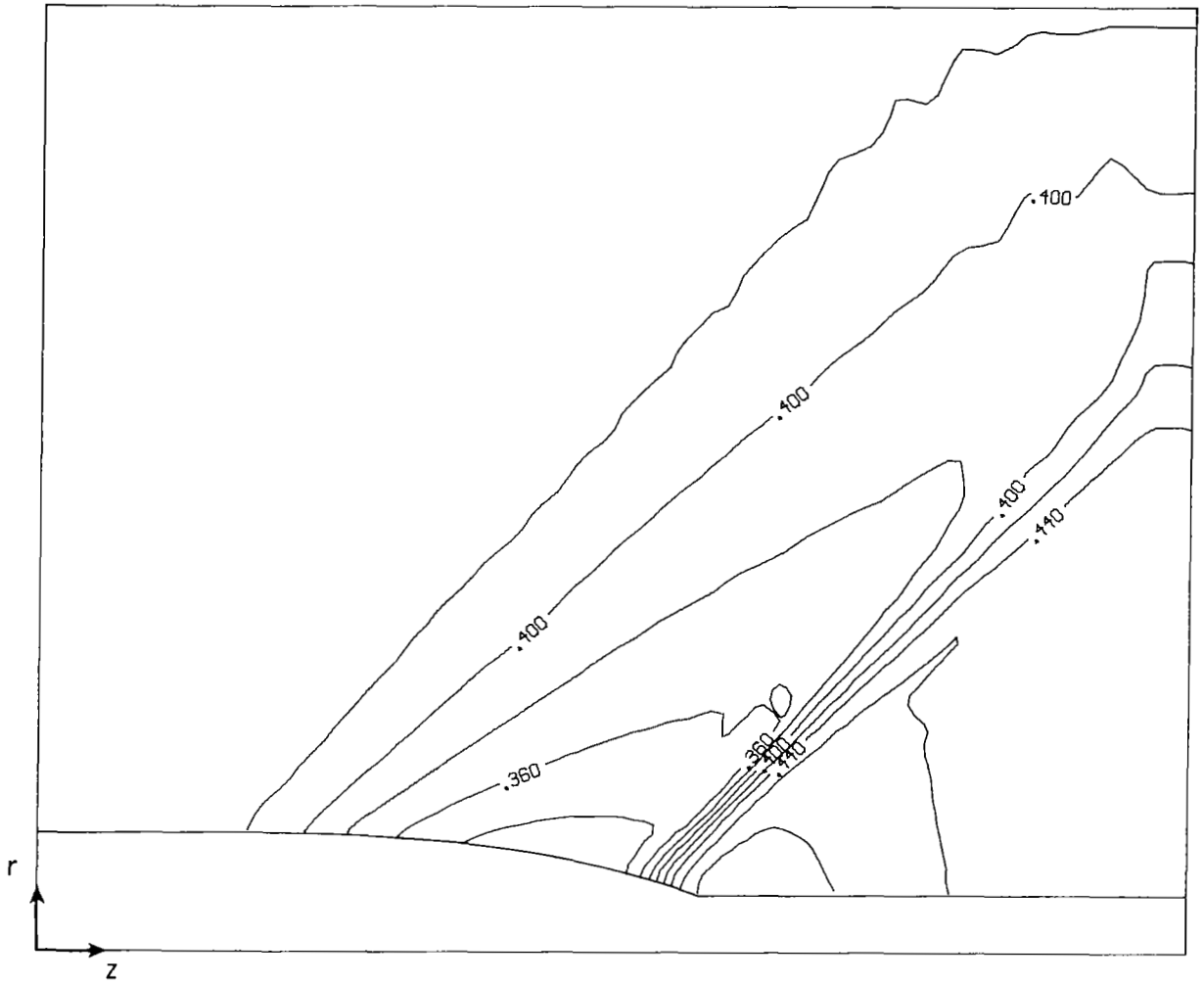Figure 6.- Surface C_p distribution for configuration 3. $M_\infty = 0.8$.
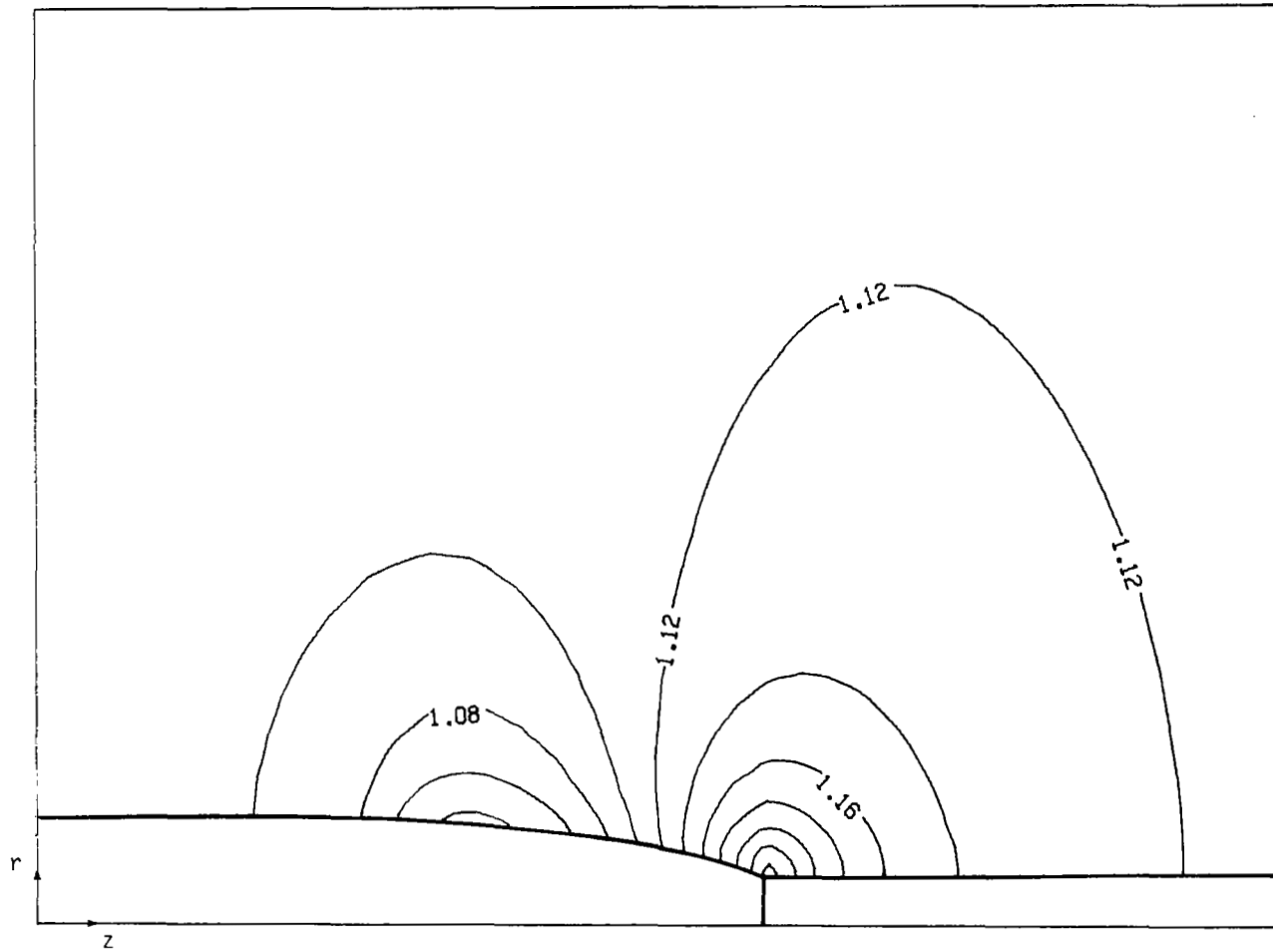
Figure 7.- Pressure contour plot for configuration 3. $M_\infty = 0.8$; contour from 1.02 to 1.24; contour interval is 0.02.
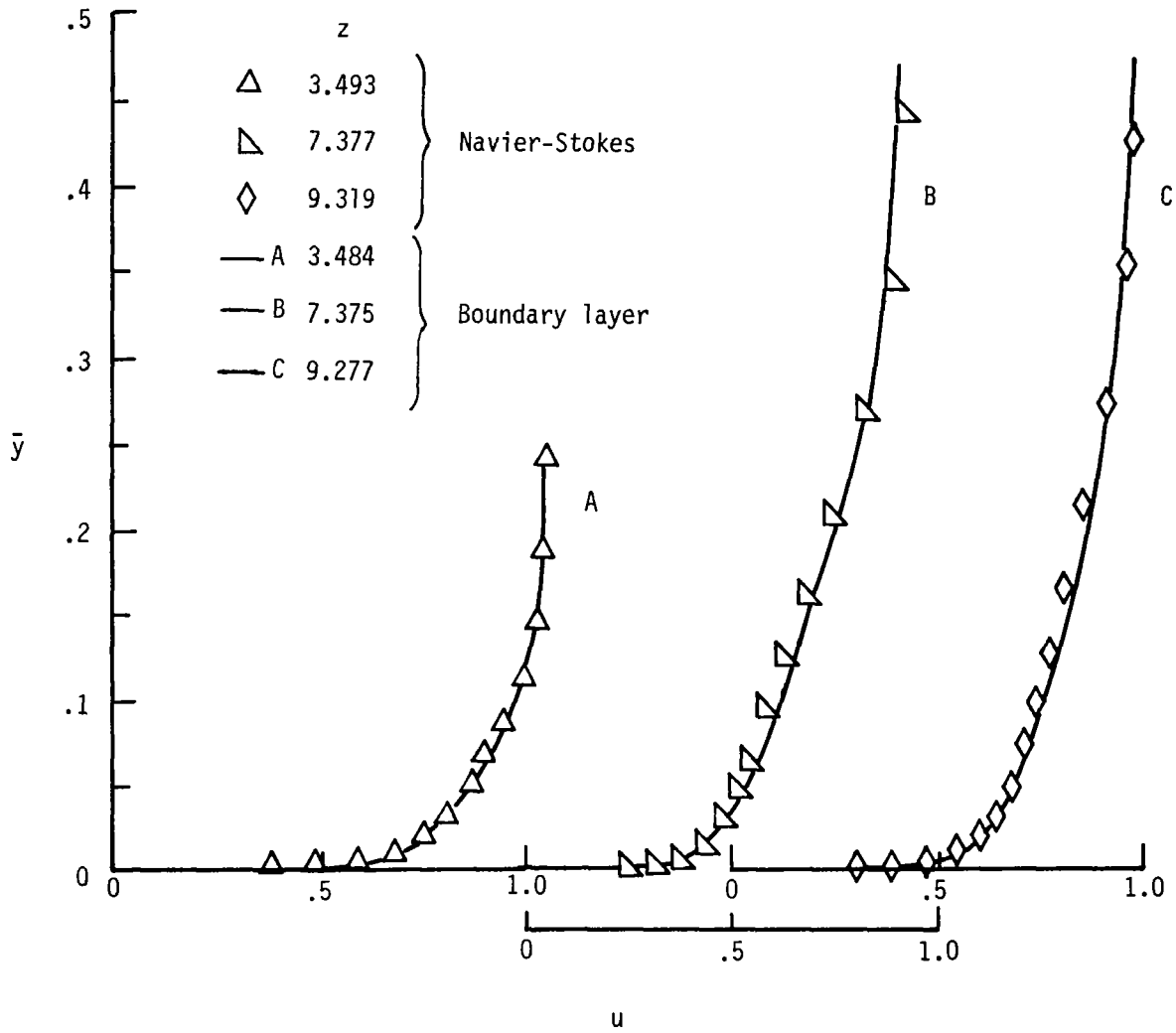
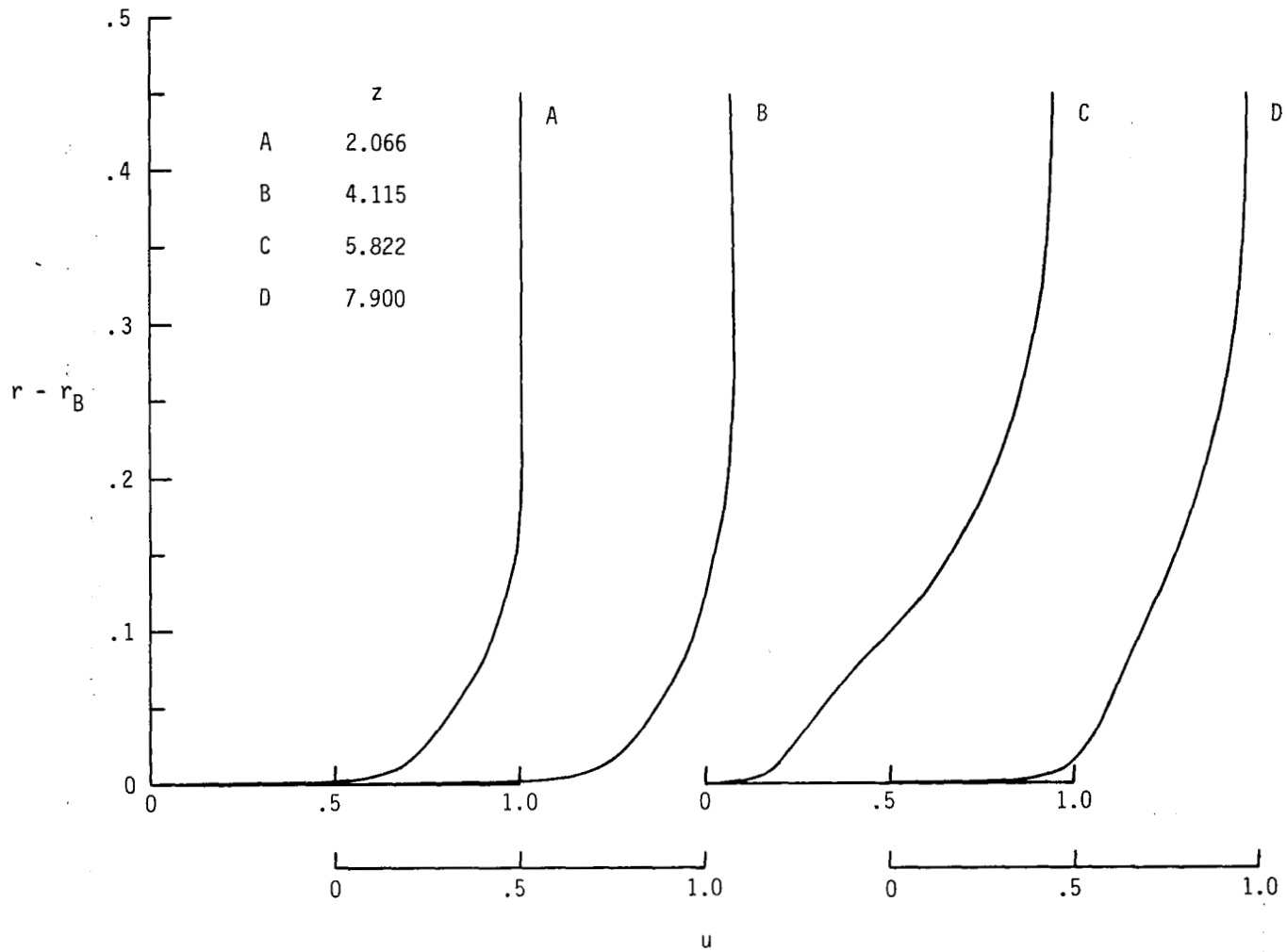Figure 8.- A comparison of velocity profiles for afterbody configuration 3. $M_\infty = 0.8$.
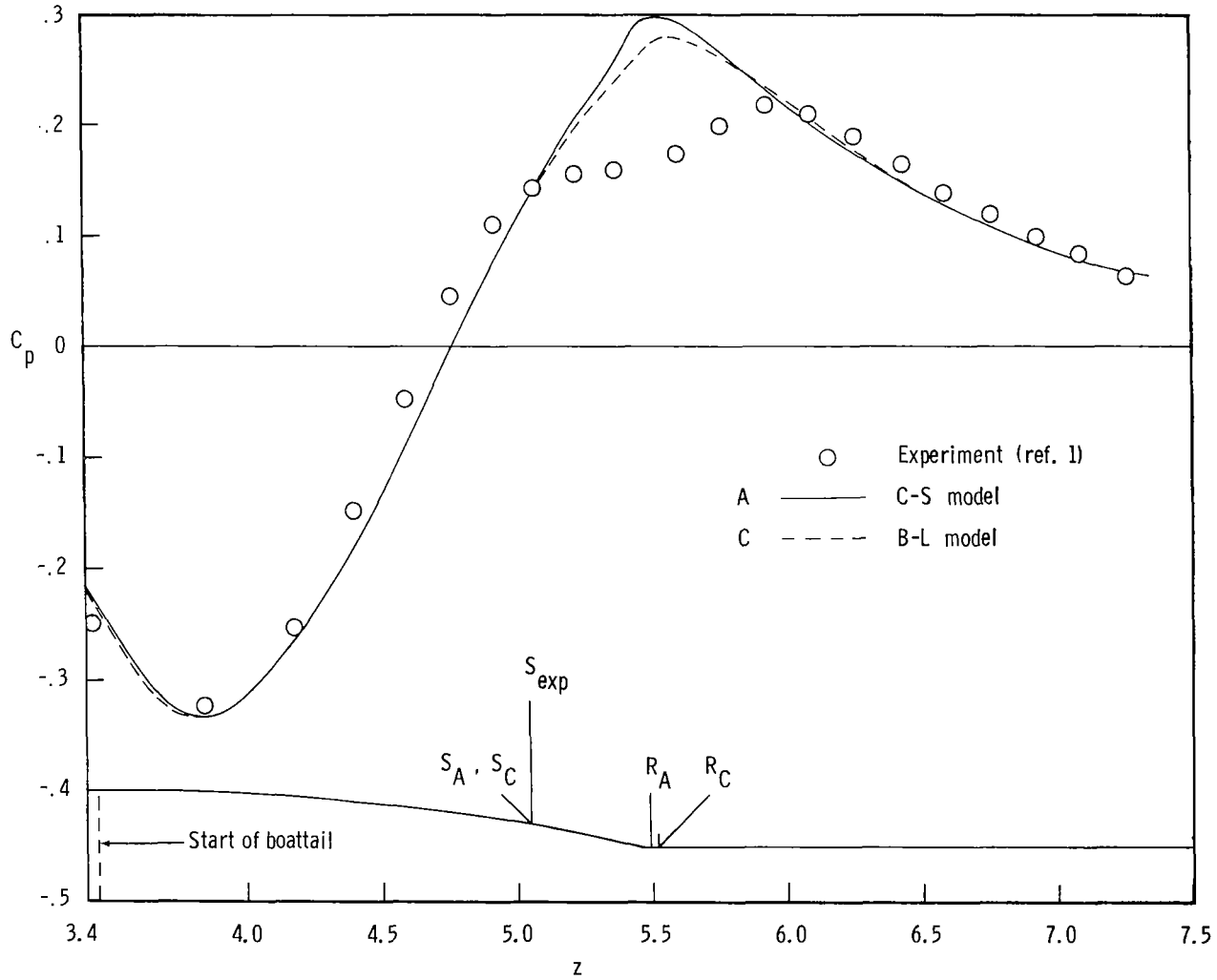
Figure 9.- Surface C_p distribution for configuration 2. $M_\infty = 0.8$.
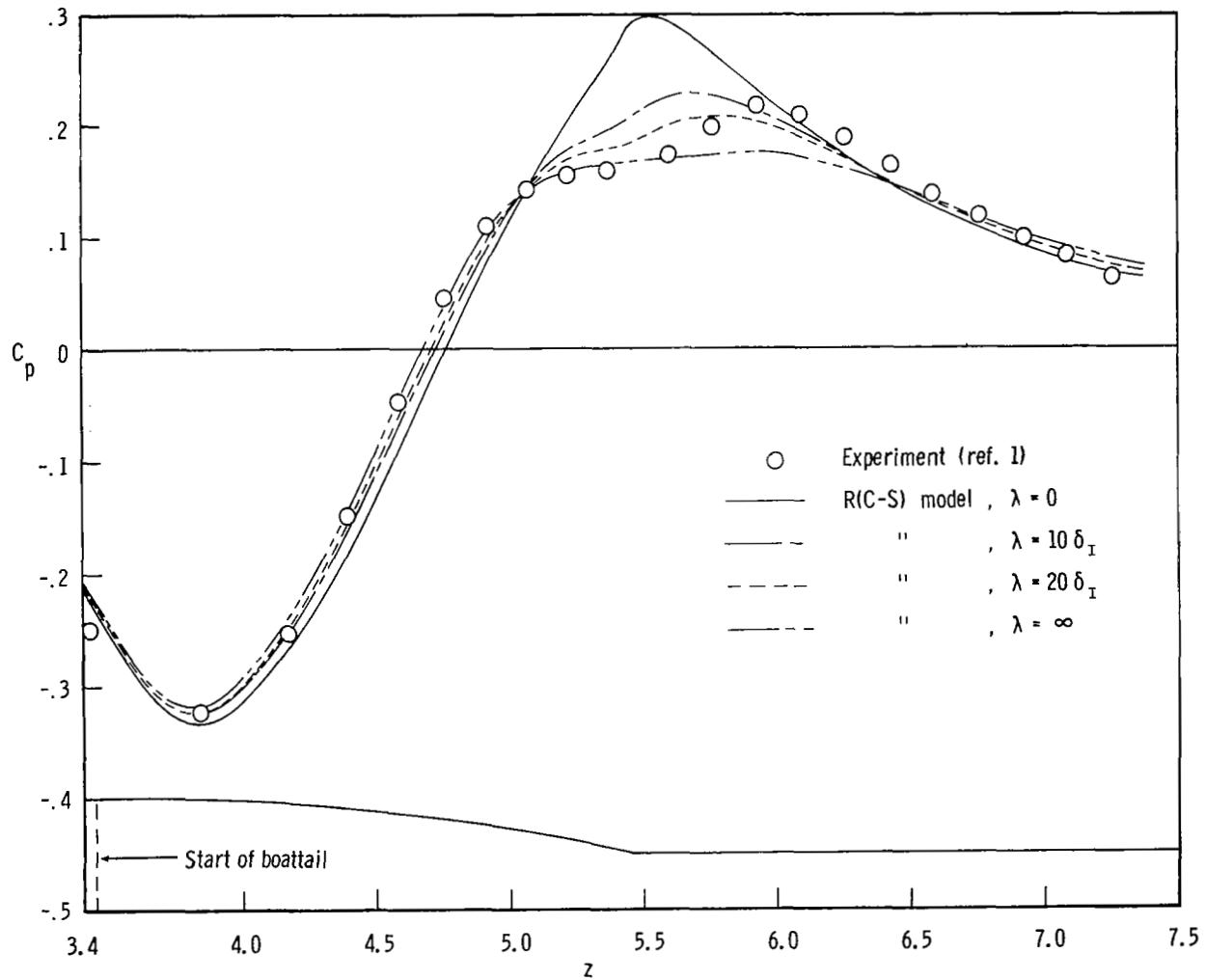
Figure 10.- Influence of relaxation on surface C_p distribution for configuration 2. $M_\infty = 0.8$.
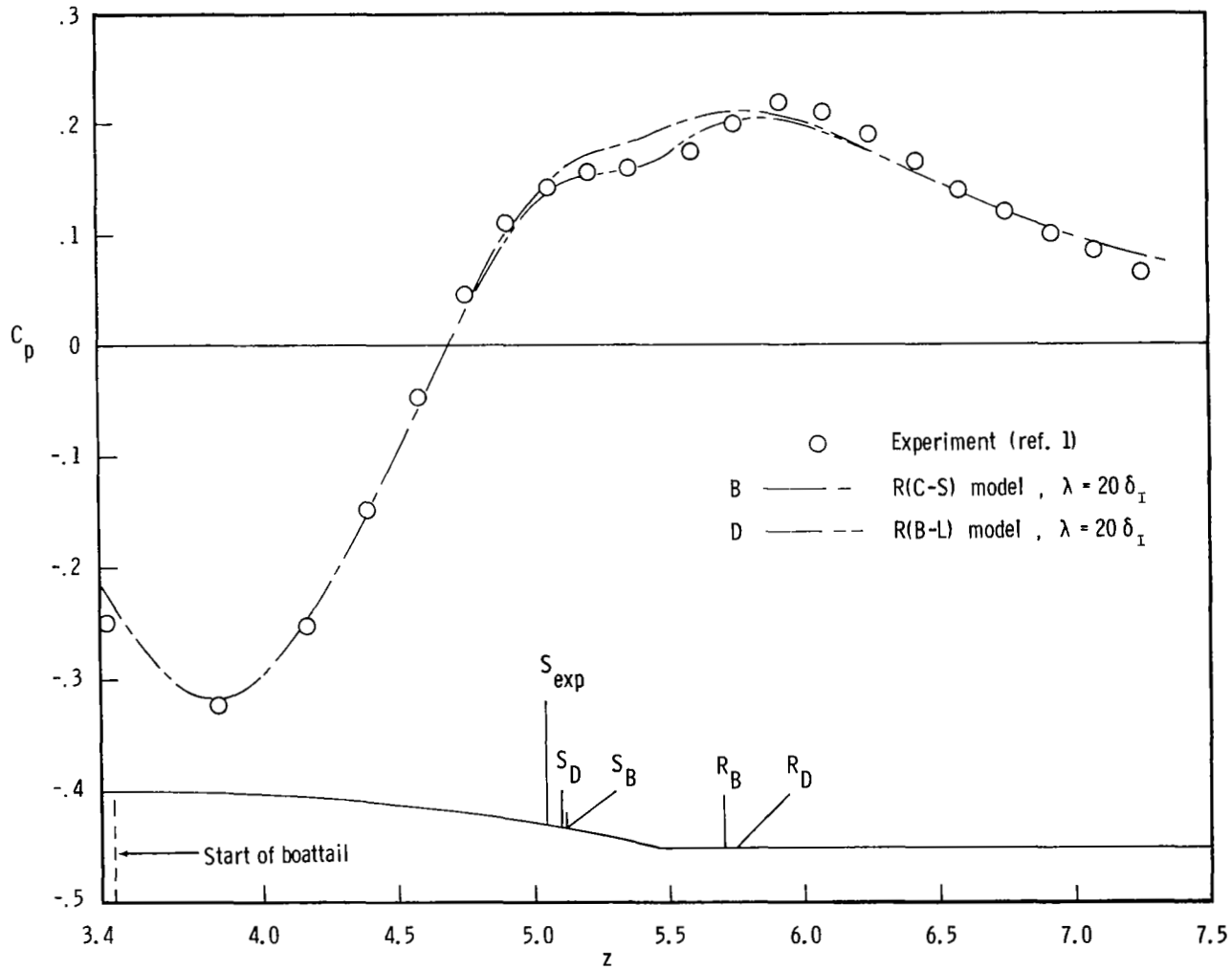
Figure 11.- Surface C_p distribution for configuration 2 using relaxation models. $M_\infty = 0.8$.
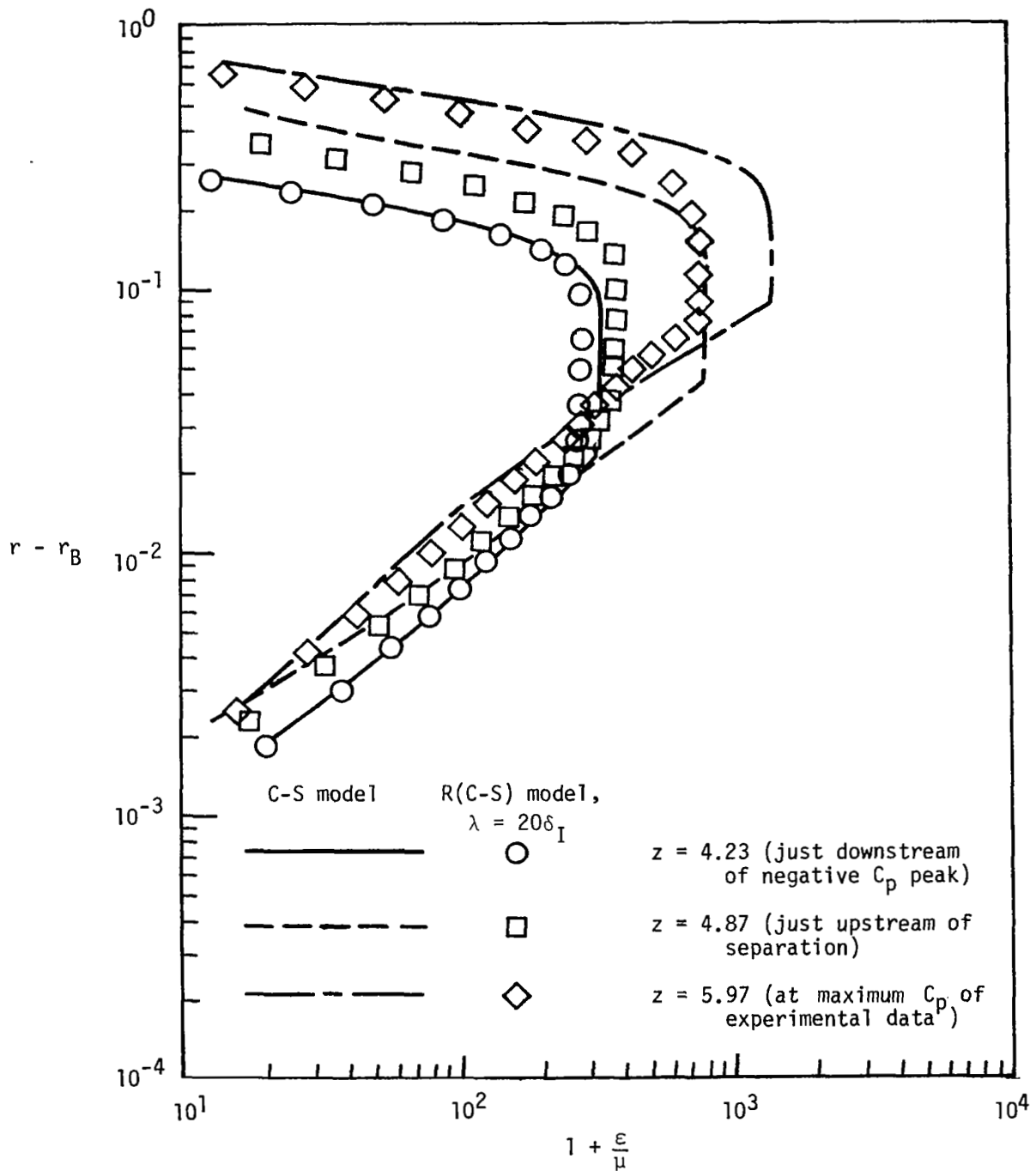
Figure 12.- Comparison of eddy-viscosity profiles for
configuration 2. $M_\infty = 0.8$.
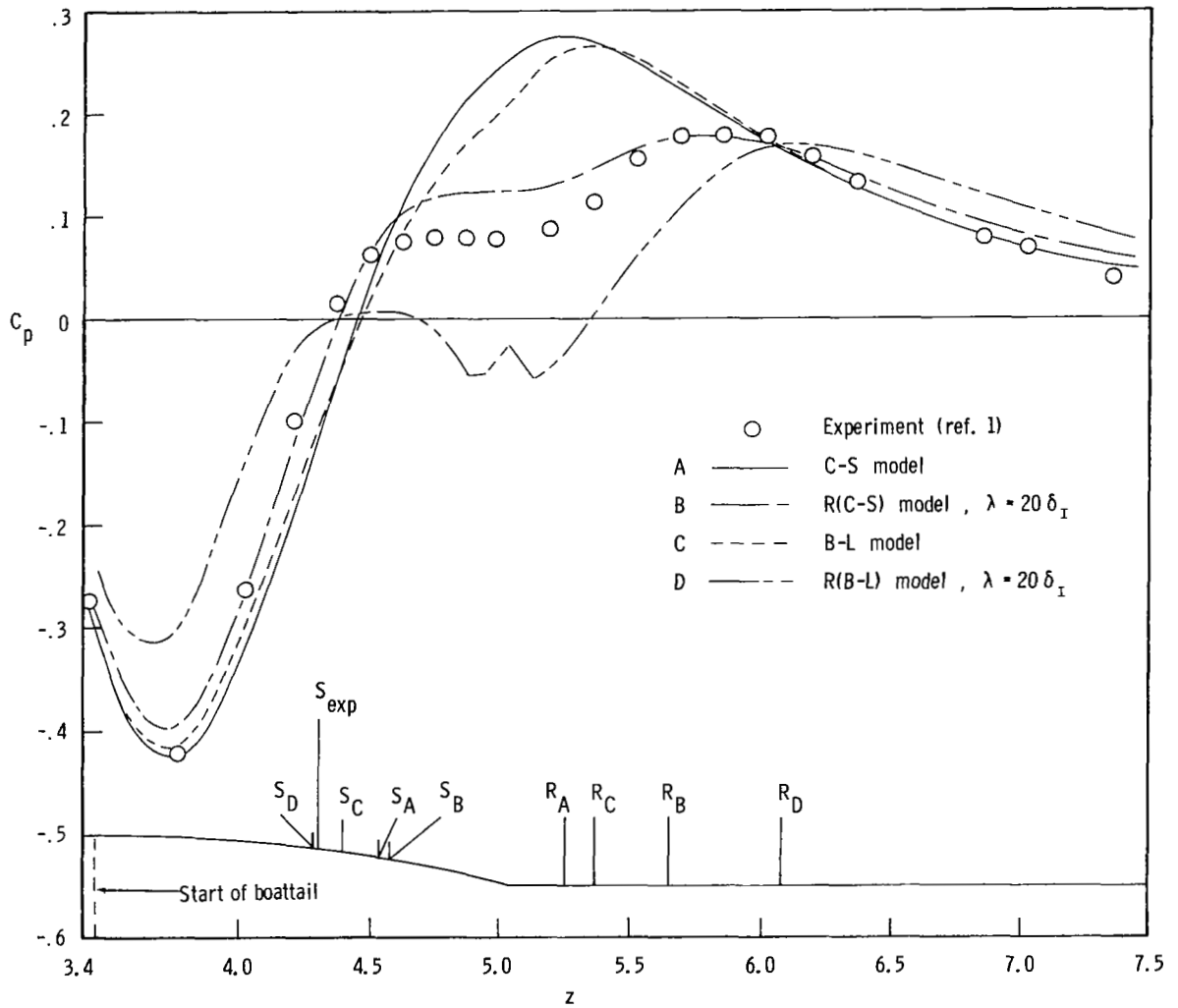
Figure 13.- Surface C_p distribution for configuration 1. $M_\infty = 0.8$.

Figure 14.- Pressure contour plot for configuration 1. $M_\infty = 0.8$; contour from 0.90 to 1.20; contour interval is 0.02.
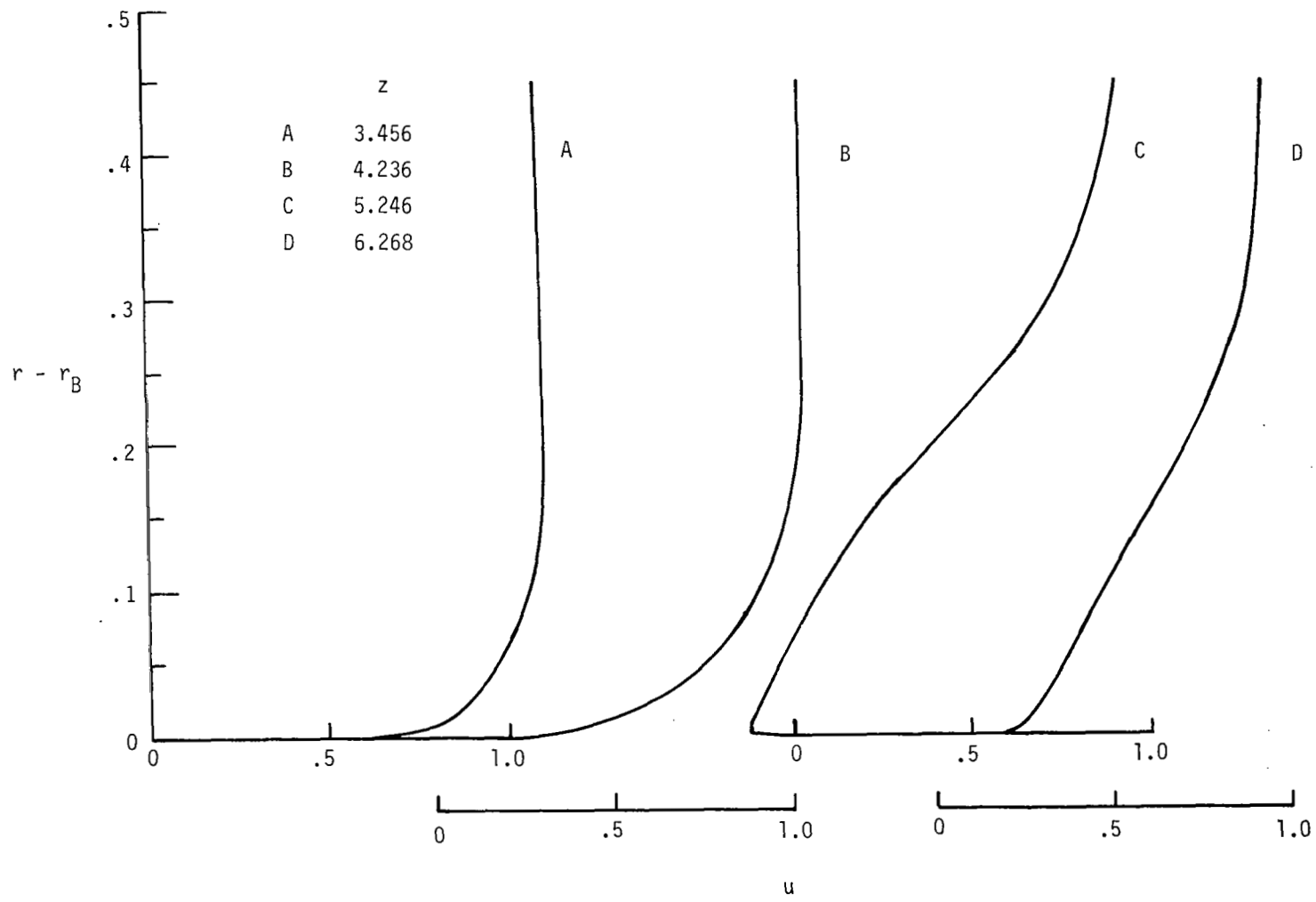
Figure 15.- Velocity profiles for afterbody configuration 1. $M_\infty = 0.8$.
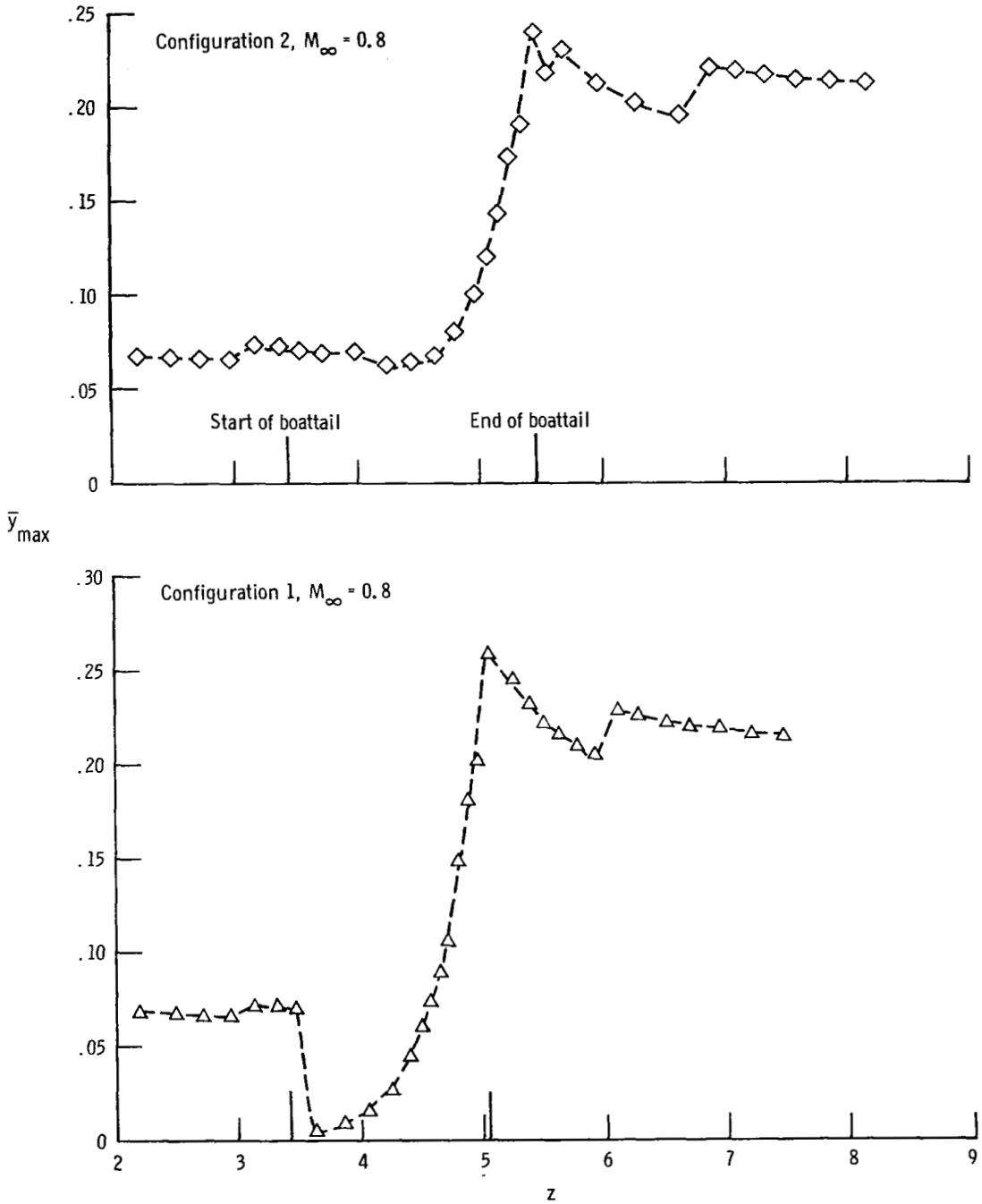
Figure 16.- Variation of $\bar{y}_{max}$ ($\bar{y}$ at F_{max}) with z.
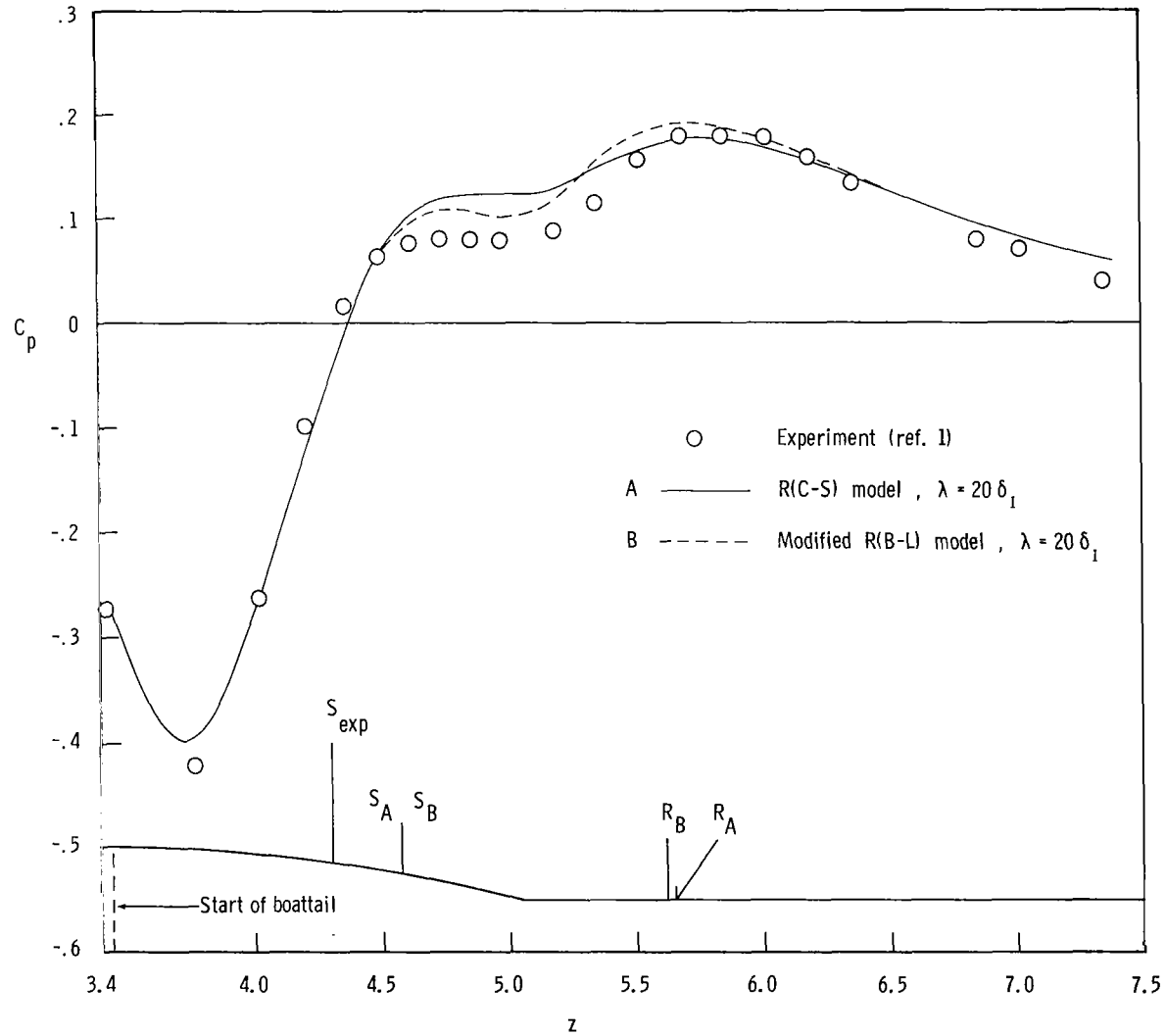
Figure 17.- Comparison of surface C_p distributions for configuration 1 using R(C-S) model and modified R(B-L) model. $M_\infty = 0.8$.
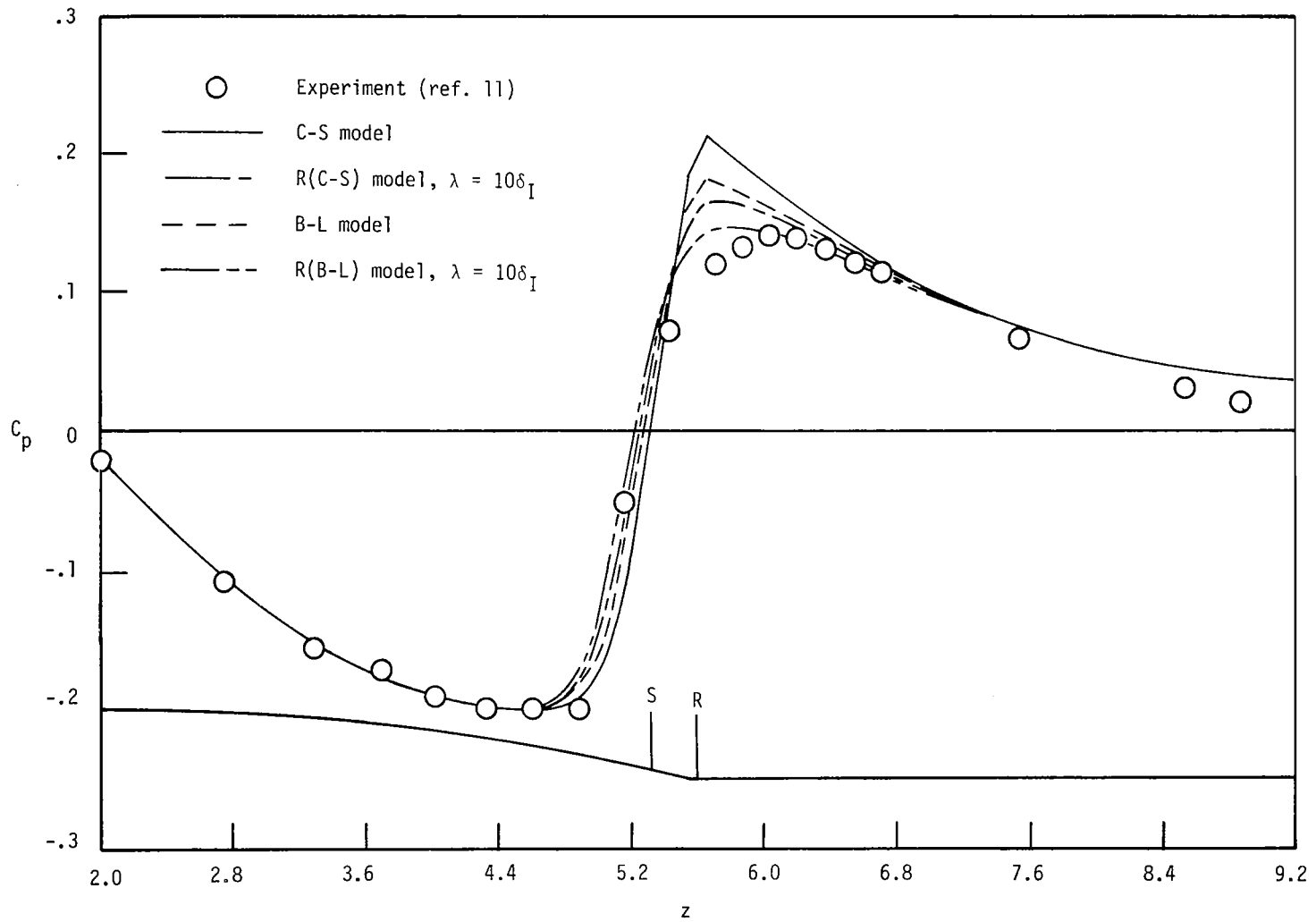
Figure 18.- Surface C_p distribution for configuration 3. $M_\infty = 1.3$.

Figure 19.- Pressure contour plot for configuration 3. $M_\infty = 1.3$;
contour from 0.32 to 0.48; contour interval is 0.02.

Figure 20.- Velocity profiles for afterbody configuration 3. $M_\infty = 1.3$.
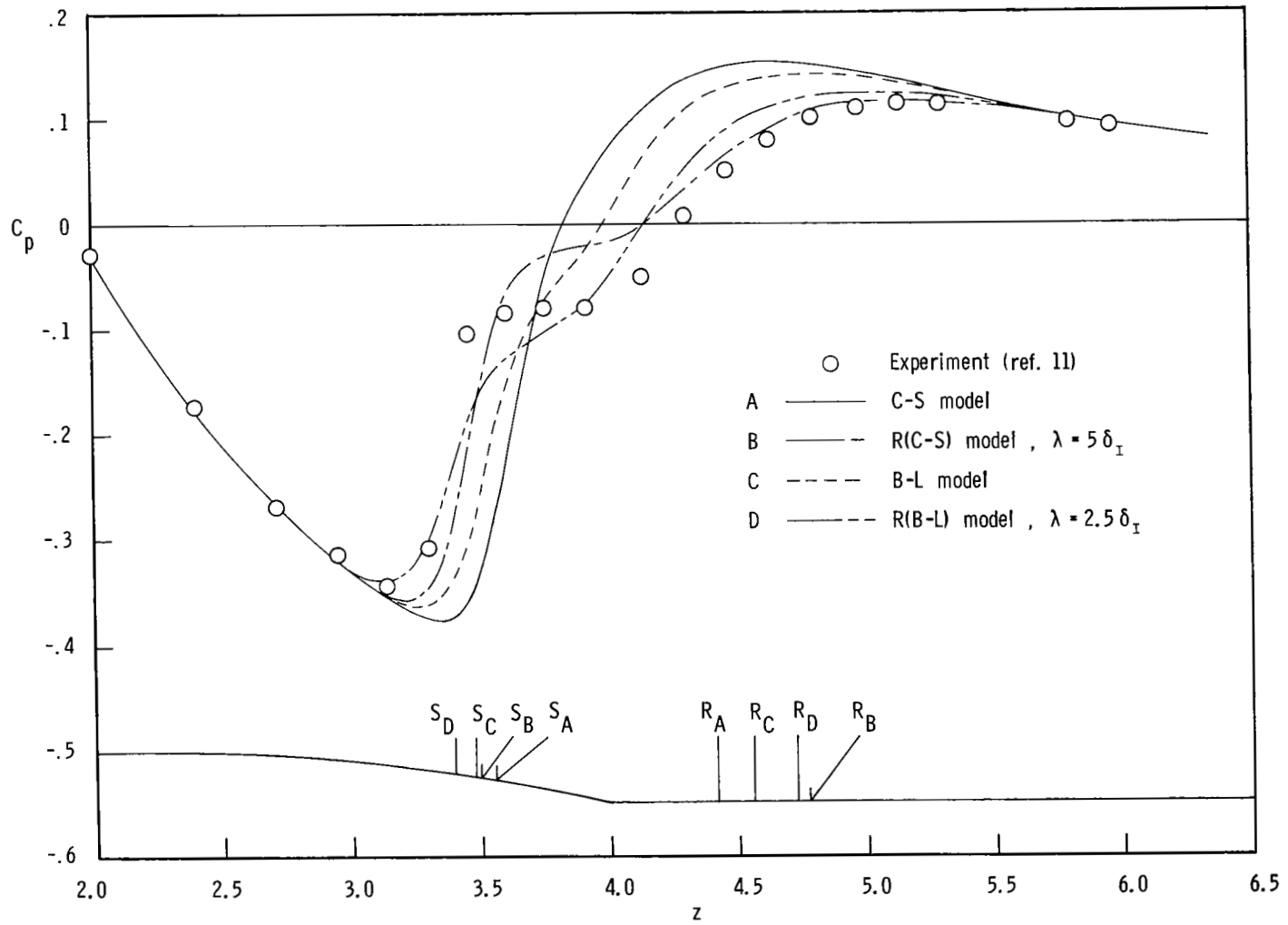
Figure 21.- Surface C_p distribution for configuration 2. $M_\infty = 1.3$.
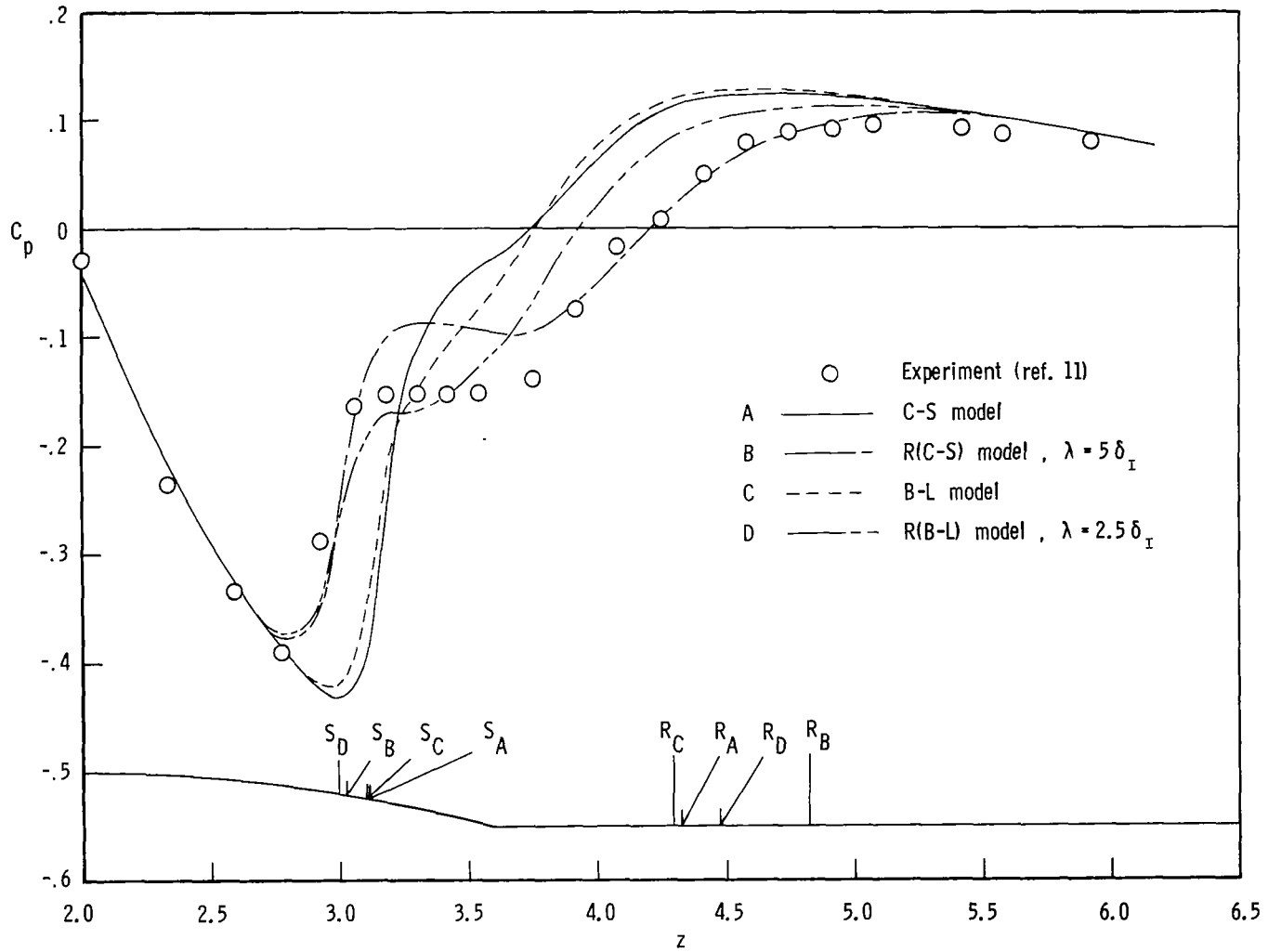
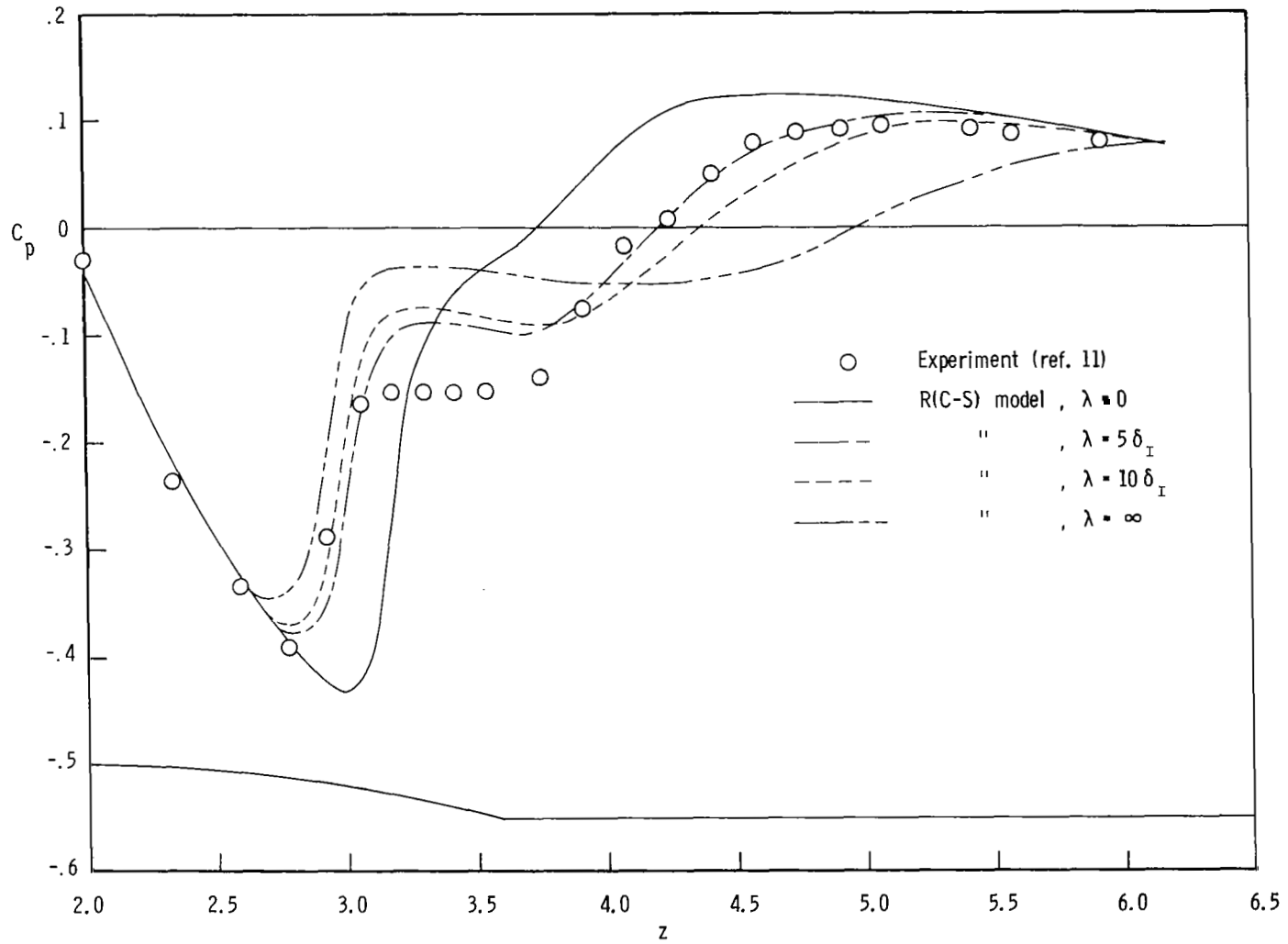Figure 22.- Surface C_p distribution for configuration 1. $M_\infty = 1.3$.

Figure 23.- Influence of relaxation on surface C_p distribution for configuration 1.
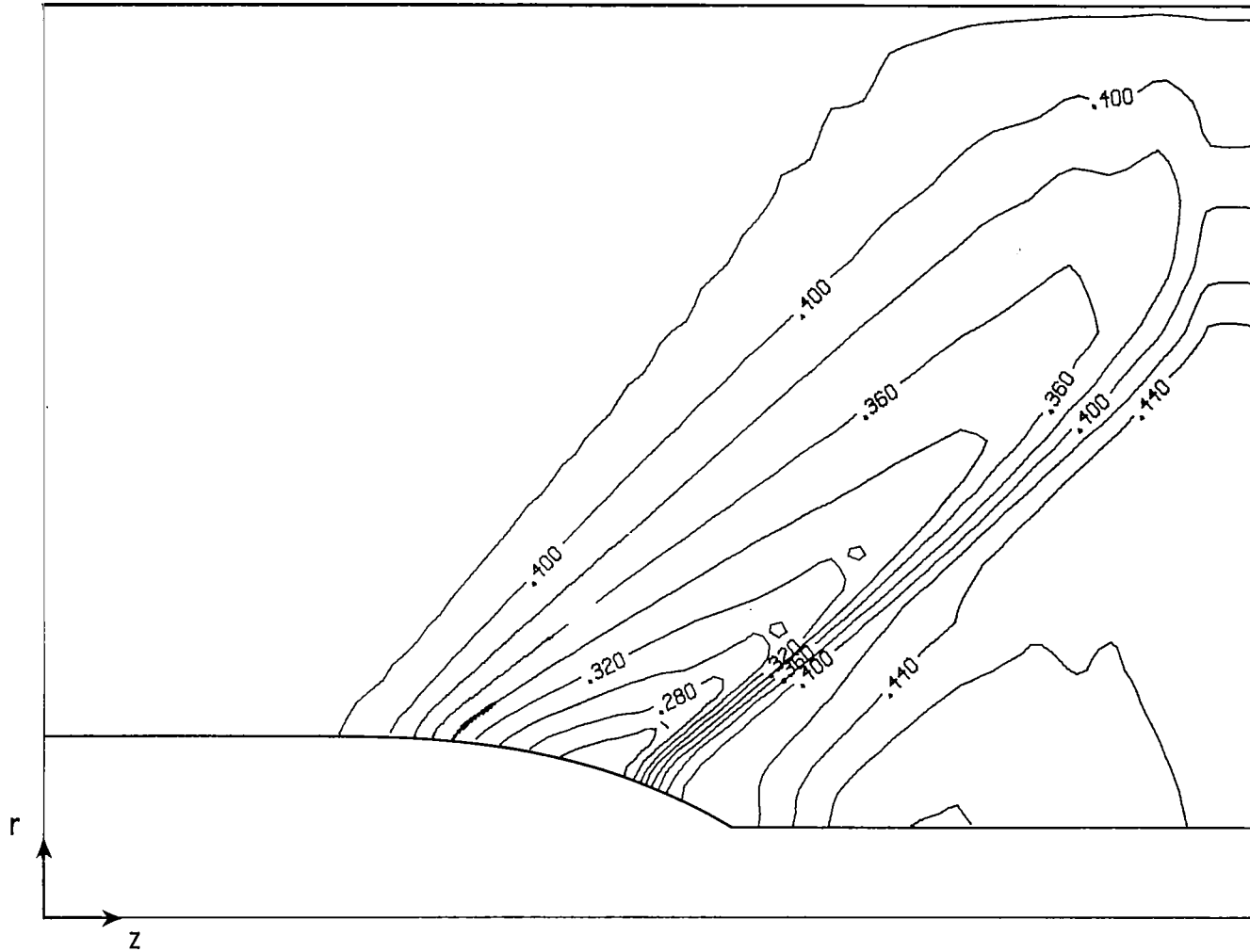$M_\infty = 1.3$.

Figure 24.- Pressure contour plot for configuration 2. $M_\infty = 1.3$; contour from 0.24 to 0.48; contour interval is 0.02.
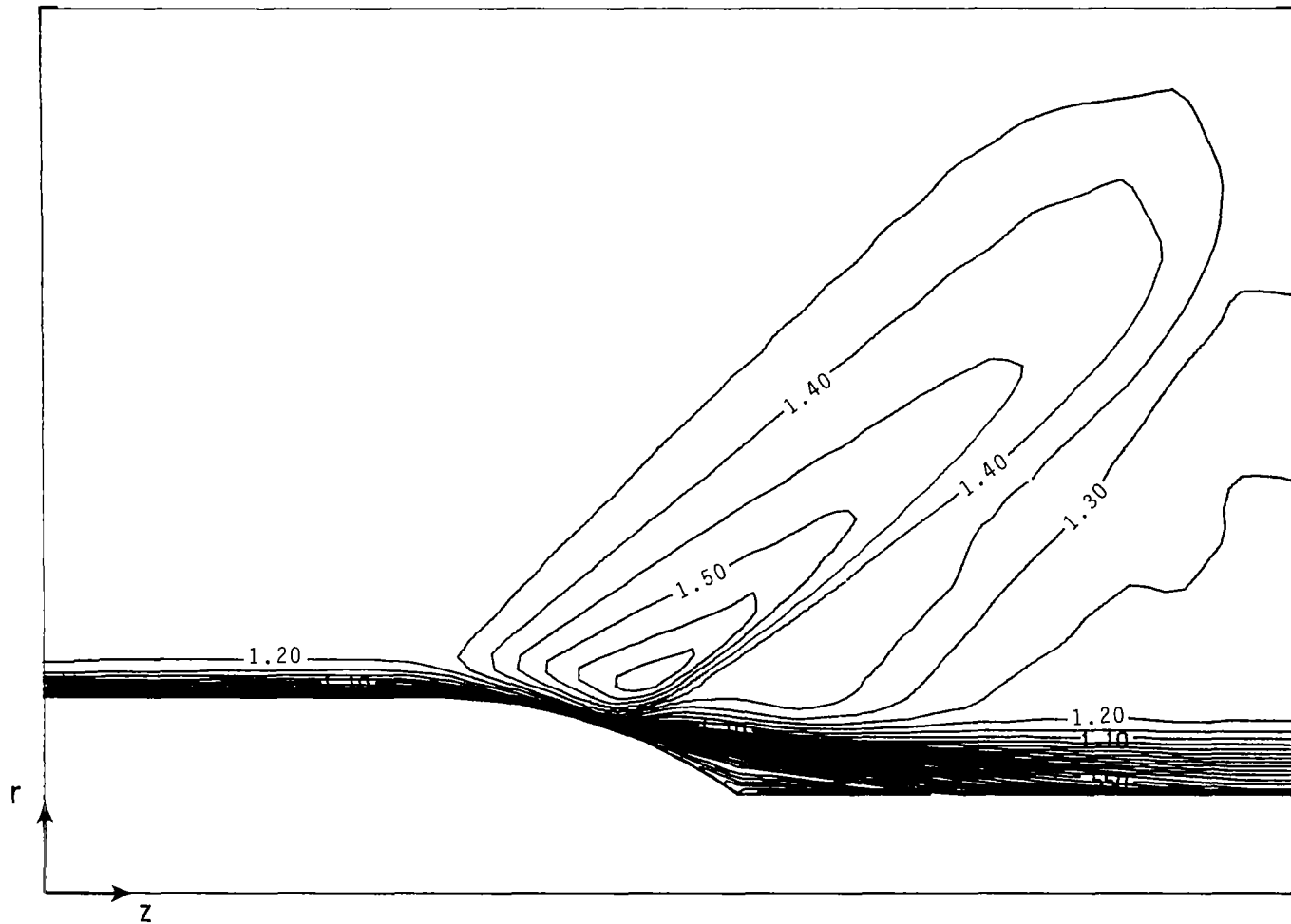
Figure 25.- Mach number contour plot for configuration 1. M_∞ = 1.3; contour
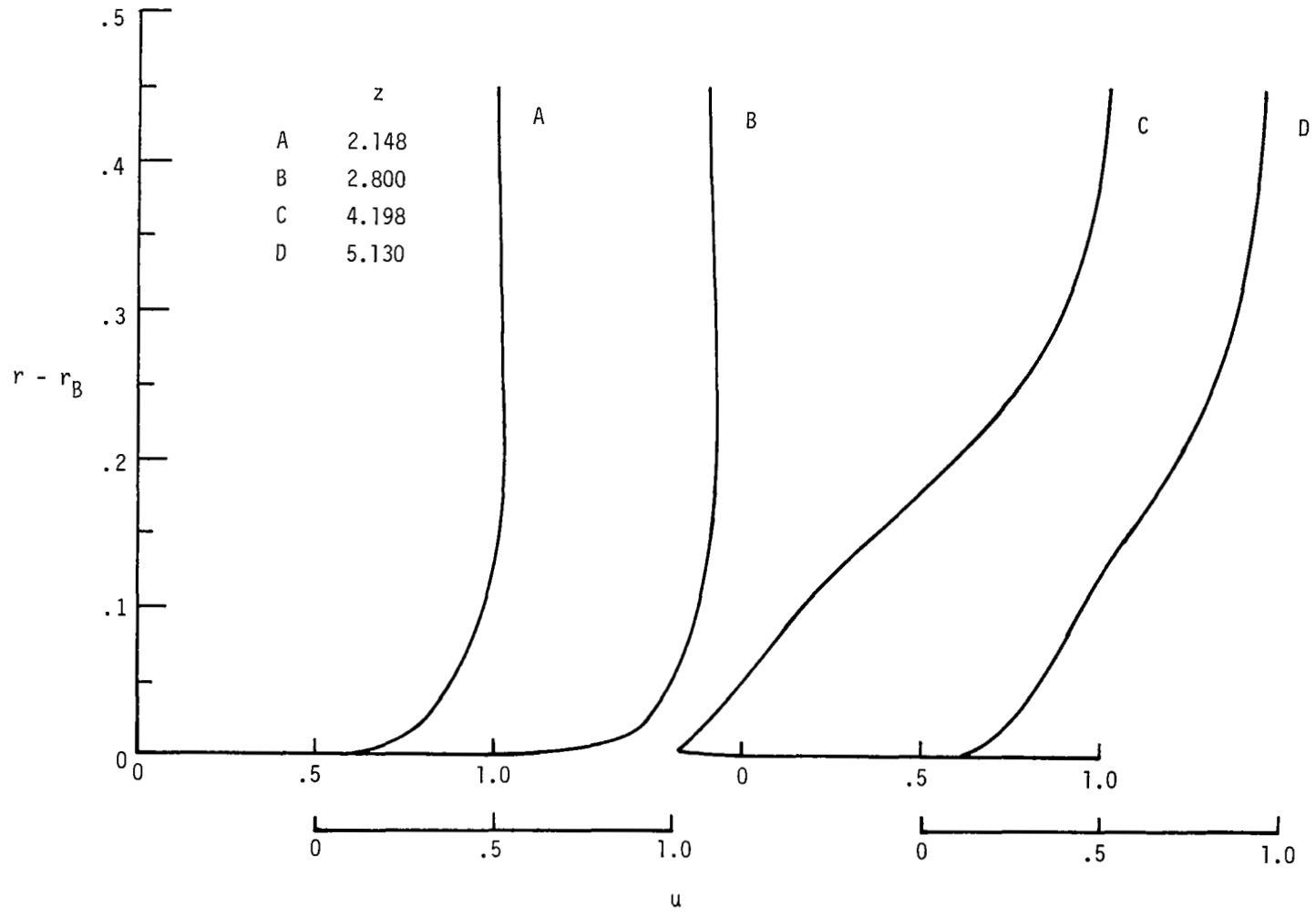from 0 to 1.60; contour interval is 0.05.

Figure 26.- Velocity profiles for afterbody configuration 1. $M_\infty = 1.3$.

1. Report No. NASA TP-1784	2. Government Accession No.	3. Recipient's Catalog No.
4. Title and Subtitle NUMERICAL SOLUTIONS OF THE NAVIER-STOKES EQUATIONS FOR TRANSONIC AFTERBODY FLOWS		5. Report Date December 1980
		6. Performing Organization Code 505-32-13-11
7. Author(s) R. Charles Swanson, Jr.		8. Performing Organization Report No. L-13826
		10. Work Unit No.
9. Performing Organization Name and Address NASA Langley Research Center Hampton, VA 23665		11. Contract or Grant No.
		13. Type of Report and Period Covered Technical Paper
12. Sponsoring Agency Name and Address National Aeronautics and Space Administration Washington, DC 20546		14. Sponsoring Agency Code

15. Supplementary Notes

16. Abstract

The time-dependent Navier-Stokes equations in mass-averaged variables are solved for transonic flow over axisymmetric boattail-plume simulator configurations. Numerical solution of these equations is accomplished with the unsplit explicit finite-difference algorithm of MacCormack. A grid subcycling procedure and computer code vectorization are used to improve computational efficiency. The two-layer algebraic turbulence models of Cebeci-Smith and Baldwin-Lomax are employed for investigating turbulence closure. Two relaxation models based on these baseline models are also considered. Results in the form of surface-pressure distributions for three different circular-arc boattails at two free-stream Mach numbers ($M_\infty = 0.8$ and 1.3) are compared with experimental data. The pressures in the recirculating flow region for all separated cases are poorly predicted with the baseline turbulence models. Significant improvements in the predictions are usually obtained by using the relaxation models.

17. Key Words (Suggested by Author(s)) Navier-Stokes Transonic Afterbody Turbulence models	18. Distribution Statement Unclassified - Unlimited Subject Category 02

19. Security Classif. (of this report) Unclassified	20. Security Classif. (of this page) Unclassified	21. No. of Pages 57	22. Price A04